Journal of Energy Storage 169 (2026) 122696

Contents lists available at ScienceDirect

Journal of Energy Storage

journal homepage: www.elsevier.com/locate/est

Research Papers

Tuning the effective thermal conductivity and thermal response of Triply Periodic Minimal Surface-based composites through anisotropic geometry rescaling

Matteo Molteni [a,*], Anna Pandolfi [b], Elisabetta Gariboldi [a]

[a] Politecnico di Milano, Department of Mechanical Engineering, Via La Masa 1, 20156, Milan, Italy
[b] Politecnico di Milano, Department of Civil and Environmental Engineering, Piazza Leonardo da Vinci 32, 20133, Milan, Italy

ARTICLE INFO

Keywords:
Phase Change Material (PCM)
Triply Periodic Minimal Surface (TPMS)
Effective thermal conductivity tensor
Additive manufacturing

ABSTRACT

This study investigates how the thermal conductivity of geometrically symmetric composites can be tuned by means of anisotropic rescaling operations. The composites addressed here are formed by filling Triply Periodic Minimal Surfaces (TPMS) lattice structures—characterized by high surface area and minimal curvature— with Phase Change Materials (PCMs). When the geometry of the lattice is modified via rescaling along a specific direction, the effective thermal conductivity tensor of the composite becomes anisotropic, favoring heat transfer along specific axes. This feature offers the possibility to preferentially drive heat fluxes to obtain more responsive systems for thermal management as in the case of PCMs.

Finite element simulations of heat conduction are performed to evaluate the influence of geometric rescaling and porosity on the diagonal components of the composite's effective thermal conductivity tensor. Lattices made of highly conductive AlSi7Mg alloys, filled with either inorganic (Sn) and organic (paraffin) PCMs, are analysed for their potential in thermal energy management applications. Results show that anisotropic geometry rescaling can significantly alter thermal conductivity, particularly at low rescaling levels. The degree of enhancement depends on the choice of materials and the level of porosity. Analytical relationships are derived linking thermal conductivity with the extent of rescaling and the porosity of the composite PCM (C-PCM).

Further, to test the effectiveness of thermal conductivity enhancement, transient regime analyses on different rescaled structures filled by the organic PCM are performed considering either linear temperature ramp or constant heat flow. The simulation results show that increasing the rescaling level accelerates PCM melting and therefore promotes faster heat storage, causing at the same time increased temperature inhomogeneities within the PCM domain. The study provides a new quantitative mapping of anisotropy as a function of scaling level and porosity and identifies topology-dependent responses to geometric stretching. The results highlight the trade-off between melting acceleration and temperature uniformity induced by geometric rescaling.

1. Introduction

The class of Triply Periodic Minimal Surfaces (TPMS) embraces a specific family of lattice structures, or lattices, characterized by periodic three-dimensional surfaces with ubiquitous zero mean curvature [1–5], a geometrical feature that provides the smallest surface area for a given boundary. This unique characteristic facilitates the local minimization of the structure surface energy, resulting in an increased surface exchange area. In an orthonormal reference system of coordinates (x, y, z), the topology of TPMS is defined by level-set equations in the form $\emptyset(x, y, z) = c$. The left-hand term is a function of the coordinates, usually involving sums of trigonometrical functions (Table 1), that describes the lattice micro-structure, while the right-hand term is the offset of the structure surface with respect to the bare one ($c = 0$), referred as the Level-set constant. The specific equations for the most representative TPMS structures on which the current study focuses, are listed in Table 1; the corresponding shapes are shown in Fig. 1.

The geometric parameters L_x, L_y and L_z in the equations of Table 1 define the size of the TPMS unitary cell in the three spatial directions. Nowadays, TPMS structures are easily produced with Additive Manufacturing (AM) techniques, which are free of technological constrains typical of the conventional manufacturing processes and allow the attainment of complex shapes and topologies using a bottom up

---

* Corresponding author.
E-mail addresses: matteo1.molteni@polimi.it (M. Molteni), anna.pandolfi@polimi.it (A. Pandolfi), elisabetta.gariboldi@polimi.it (E. Gariboldi).

https://doi.org/10.1016/j.est.2026.122696
Received 17 June 2025; Received in revised form 16 March 2026; Accepted 11 May 2026

Nomenclature

AM	Additive Manufacturing
c	Level-set constant
C_p	Specific heat at constant pressure [$Jkg_{-1}K$-1)]
C-PCM	Composite Phase Change Materials
D	Diamond
G	Gyroid
h	Maximum meshing element size [mm]
I	I-Graph and wrapped package-graph
i	Index related to the i^{-th} direction
j	Index related to the j^{-th} direction
K_{ij}	Components of the thermal conductivity tensor [Wm^{-1} K_{-}^{1}]
$k_{eff,i}$	Effective thermal conductivity along i-direction [Wm^{-1} K_{-}^{1}]
$K_{\parallel}$	Parallel thermal conductivity (upper Wiener bound) [Wm^{-1} K_{-}^{1}]
$K_{\perp}$	Series thermal conductivity (lower Wiener bound) [Wm^{-1} K_{-}^{1}]
k_1	Effective thermal conductivity of the filling phase (alternatively, C80 paraffin of Sn)
k_2	Effective thermal conductivity of the lattice skeleton type (AlSi10Mg)
j	Index related to the j-th direction
L_i	Original TPMS cell size along i-directions [mm]
l_z	Length of the rescaled skeleton lattice along z direction [mm]
N	Rescaling level of cell size along Z direction
n	Density of points
PCM	Phase Change Materials
P	Primitive-Schwarz
q_i	Average normal heat flux in i-th direction [Wm^{-2}]
r	Thermal conductivity ratio [–]
RT	Room temperature (25 °C) [K]
TPMS	Triply Periodic Minimal Surface
ΔT_i	Temperature difference in i-direction [K]
$\Delta T_{Al\text{-}PCM}$	Maximum temperature difference between the average of the metallic and PCM domains [K]
t_i	Time at the onset of PCM melting [s]
t_f	Time at the completion of PCM melting [s]
ε	Porosity
η_i	Microstructural efficiency in i-direction
λ	Index related to the λ-th phase
ρ	Density [kg/m^3]
$\overline{\rho}$	Relative density [kg/m^3]
μ_i	Morphological index in i-direction

Table 1
Mathematical definition of the TPMS structures considered in this study.

TPMS structure name	TPMS structure mathematical expression
Primitive-Schwarz (P)	$\cos\left(\frac{2\pi}{L_x}x\right)+\cos\left(\frac{2\pi}{L_y}y\right)+\cos\left(\frac{2\pi}{L_z}z\right)=c$
Gyroid (G)	$\sin\left(\frac{2\pi}{L_x}x\right)\cos\left(\frac{2\pi}{L_y}y\right)+\sin\left(\frac{2\pi}{L_y}y\right)\cos\left(\frac{2\pi}{L_z}z\right)+\sin\left(\frac{2\pi}{L_z}z\right)\cos\left(\frac{2\pi}{L_x}x\right)=c$
Diamond (D)	$\sin\left(\frac{2\pi}{L_x}x\right)\sin\left(\frac{2\pi}{L_y}y\right)\sin\left(\frac{2\pi}{L_z}z\right)+\sin\left(\frac{2\pi}{L_x}x\right)\cos\left(\frac{2\pi}{L_y}y\right)\cos\left(\frac{2\pi}{L_z}z\right)+\cos\left(\frac{2\pi}{L_x}x\right)\sin\left(\frac{2\pi}{L_y}y\right)\cos\left(\frac{2\pi}{L_z}z\right)+\cos\left(\frac{2\pi}{L_x}x\right)\cos\left(\frac{2\pi}{L_y}y\right)\sin\left(\frac{2\pi}{L_z}z\right)=c$
I-Graph and wrapped package-graph (I)	$\cos\left(\frac{2\pi}{L_x}x\right)\cos\left(\frac{2\pi}{L_y}y\right)+\cos\left(\frac{2\pi}{L_y}y\right)\cos\left(\frac{2\pi}{L_z}z\right)+\cos\left(\frac{2\pi}{L_z}z\right)\cos\left(\frac{2\pi}{L_x}x\right)-\cos\left(\frac{2\pi}{L_x}x\right)\cos\left(\frac{2\pi}{L_y}y\right)\cos\left(\frac{2\pi}{L_z}z\right)=c$

approach [5–7]. Moreover, the flexibility of AM permits TPMS to be manufactured in organic [6,8,9], metallic [7,10–13], or ceramic materials [14,15].

The potential of TPMS structures has been successfully explored from both numerical [1,16–18] and experimental points of view, demonstrating clear advantages with respect to the conventional lattice structures because of the superior surface-to-volume ratio. Specific applications found in the literature include wave insulation [19,20], mechanical energy absorption [11,21], catalytic processes [22,23], cell regeneration lattices [24], and heat exchange [17,25–28]. Usually, metal TPMS structures are coupled with other materials to create composites with exceptional effective properties, i.e., the ones considering the composite as a single medium, exploiting the unique characteristics of the lattice structures. A typical example in thermal field applications is the combination of TPMS lattices made of a highly thermally conductive material with a low thermally conductive material. The resulting effective thermal conductivity —representing the thermal conductivity of the entire composite seen as a homogenized medium—, referred to as k_{eff} in the following, is indeed higher than the one of the bare low thermally conductive material, as it derives from the individual properties of both phases [29]. The extent of this increase depends largely on the volume fraction of the two phases and their spatial arrangement within the composite, since the effective thermal conductivity is strongly influenced by the configuration of the phases. In this context, compared to conventional lattice structures (e.g., BCC, Kelvin), the use of TPMS topologies offers advantages in achieving composites with higher effective thermal conductivity [5,30,31]. Another possibility offered by TPMS lattices is their intrinsic feature of splitting the lattice into two distinct and non-interconnected volumes. This statement led these structures to be considered for heat exchangers [8] and heat sinks [32]. In general, for heat exchanger purposes, metallic TPMS structures are usually combined with air [8,12], water [8,18,27], or other working fluid media [17]. By quantifying the heat transfer rate and the pressure drop offered by Gyroid structures, Reynolds et al. [8] proved the clear advantages of their utilization in the design of microchannel air and water-based heat exchangers. Attarzadeh et al. [17], Alteneiji et al. [18], and Oh et al. [27] proposed methodologies for the quantification of the design parameters of TPMS-based heat exchangers. Catchpole-Smith et al. [12] quantified experimentally the effective thermal conductivity of TPMS-air composites manufactured via powder bed laser fusion. More recently, TPMS composites were adopted in the field of Phase Change Materials (PCMs) [33,34]. PCMs enable the storage and release of excess thermal energy through their latent heat of transformation, making them especially attractive for thermal energy management applications. Solid-liquid transformations are the most widely used, offering the best compromise between storable/releasable thermal energy and efficient volume management during phase transition. More in general, the definition of PCMs includes any type of material, ranging from organic to metals. The former benefit from high latent heat per unit mass, providing at the same time accessible transition temperatures (rarely higher than 100 °C). However, they suffer from low thermal conductivity, which severely limit their performances.

This challenge can be easily addressed by choosing metallic PCMs, whose thermal conductivity is up to three orders of magnitude higher than the one of organics. Moreover, they exhibit high latent heat per unit volume, but low storage capacity per unit mass and pose challenges in handling when molten, due to their reactivity and corrosiveness [35]. In this regard, the introduction of other phases to build composite materials represents a powerful strategy for the realization of composite PCMs (C-PCMs) with outstanding properties in both cases. As far as the organic PCMs are concerned, their percolation through highly thermally conductive skeletons, typically made of metal [36–38], among which Al and Cu, demonstrates to be effective in raising the PCM transformation rate. On the other hand, focusing on metallic PCMs, corrosiveness can be mitigated by selecting properly immiscible metallic systems, composed of at least two different elements that do not interact in either the solid or liquid state, thus preserving the integrity of the device [39]. Typical examples are Al—Sn and Cu—Fe, systems roughly definable as composites, as they consist of phases whose composition closely matches that of the pure elements. The low-melting metal serves as the active PCM, undergoing melting and solidification, while the high-melting metal functions as passive, stable matrix.

In both cases, the arrangement of the two phases within the resulting composite determines its overall thermal conductivity [40], and consequently, the performances of the C-PCM. Indeed, efficiently driving heat fluxes toward the PCM determines its response fastness and the related storage/release capability. As previously presented, the proper selection of high thermally conductive phases in the composite can be adopted as a first strategy to foster the C-PCMs to higher and faster performances [41].

However, beyond the bare material choice, other approaches, which focus on the engineering of the high thermally conductive supporting structure, have recently taken off, among which promoting anisotropic heat transfer. This feature favours heat transport along specific directions, so that with proper design of the Thermal Energy Storage or Thermal Energy Management systems containing the composite, high heat fluxes can be preferentially guided within the composite.

In practical TES systems, thermal loading is typically directional, imposed by boundary heat fluxes or embedded heat exchangers, thus the ability to actively tune directional effective thermal conductivity becomes more important than simply maximizing the isotropic average conductivity [42]. Anisotropic thermal transport can be promoted in the materials via both intrinsic and extrinsic mechanisms. The former is typical of materials with complex crystallographic structures [43] or bonds of different nature [44]. The latter on the other hand consists in the introduction of defects addressed toward hindering the thermal transport in specific directions [45] or other highly thermally conductive phases able to promote preferential oriented path within the material itself [46]. The application of external fields, either of magnetic [47] or mechanical nature [48,49], is assessed to be another valuable tool for the promotion of anisotropy in thermal transport. Besides anisotropy strategies, it is worth mentioning that heat can also be guided with the means of metamaterials [50]. The need of directional heat flux finds indeed practical application, for example in Thermal Management Systems [51], especially addressed toward the localized removal of heat (electronic systems or automotive sector), or thermal recuperators, thought for cryogenic or space systems, to limit undesired heat losses [46]. In this sense, the adoption of lattice structures with tunable geometries and porosities allows to modify thermal conductivity within the structure itself, assessed both via numerical [52] and experimental way [53], including TPMS as well [12]. The same approach is adopted with the adoption of hierarchical structures as well [54].

More recently, other strategies rose in order to maximize heat transport, modifying porosity levels within the lattice itself, leading to functionally graded structures [55] or finding synergistic matches between thermal input directions and geometrical features (cross sectional areas, pore orientation) [52,56].

To the authors' best knowledge, some attempts in the literature have been already performed to evaluate the impact of anisotropy on the melting rate of PCMs. Sun et al. [57] worked on Kelvin cell, Yan et al. [58] on Diamond structure and Li et al. on BCC (Body centered cubic) [59]. All the studies are addressed toward the maximization of the hydraulic behaviour of the composite, favoring the anisotropic structures the effectiveness of the natural convection. However, the role of anisotropy in mere thermal conduction is still to be investigated. Despite the practical relevance of anisotropic heat guidance, systematic strategies to engineer and quantify anisotropic thermal transport in TPMS-based C-PCM systems remain limited, and the role of geometric rescaling as a controlled mechanism to induce directional conductivity modulation has not been sufficiently investigated. Clearly, unidirectional geometric rescaling alters ligament orientation, cross-sectional area distribution, and connectivity density along selected axes, offering a direct and manufacturable way to tailor axial versus transverse heat transport. Additionally, the relationship between scaling intensity, porosity evolution, TPMS topology, and resulting anisotropic effective conductivity has not been comprehensively quantified, and the consequences of directional rescaling on transient melting dynamics, which depart from the steady-state behaviour, remain poorly understood. In this work, we address these issues by systematically investigating unidirectional geometric rescaling as a controlled strategy to tune anisotropic effective thermal conductivity in TPMS-based composite PCM systems. We aim at defining a quantitative and topology-aware framework that links geometric scaling, porosity evolution, and directional thermal transport under both steady and transient regimes. The methodological novelty of our approach consists in applying systematic unidirectional rescaling to multiple TPMS geometries and evaluating the resulting anisotropy through finite element simulations. A dual analysis procedure is adopted, which consists in combining steady-state effective conductivity characterization with transient melting simulations under constant heat flux boundary conditions. The study outcomes include the quantitative mapping of anisotropy as a function of scaling level and porosity, the identification of topology-dependent responses to

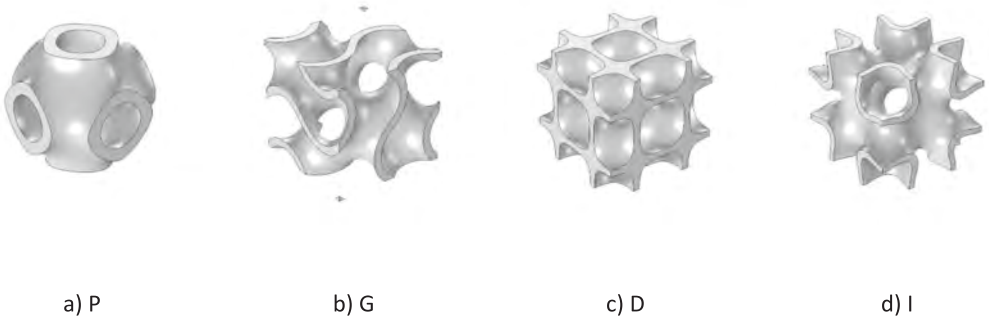

Fig. 1. Visualization of the geometry of the TPMS structures here considered: a) Primitive-Schwarz (P), b) Gyroid (G), c) Diamond (D) and d) I-wrapped-package graph (I).

geometric stretching, and the analysis of the trade-off between melting acceleration and temperature uniformity.

The target can be achieved directly selecting materials with two-dimensional structures, such as graphene or boron nitride nanosheets, which both exhibit difference of orders of magnitude between the in-plane and out-of-plane thermal conductivity [60].

Anisotropy promotion can be also achieved either introducing and aligning high thermally conductive second phases with various aspect ratios [61] or controlling the arrangement of macroscopic structure embedding low thermally conductive PCM [62].

Anisotropy achievement via introduction of properly engineered high thermally conductive phases in the resulting C-PCM can be exploited indeed to promote faster heat supply to the storage phase, i.e., PCM.

Aim of this study is to explore the possibility of modifying the properties of TPMS skeleton-based composites for preferential heat transfer by geometrically scaling the metallic skeletons in one of the principal directions of symmetry of the lattices, to attain anisotropy in thermal conductivity.

Our work complements and advances recent numerical and experimental studies that have explored heat conduction in TPMS-PCM materials proposing general enhancements and anisotropic effects. To evaluate geometry-induced directional heat transfer effects in PCM composites, lattice Boltzmann simulations have been presented in [63], revealing that anisotropic Gyroid skeletons can enhance heat exchange capacity and reduce melting time compared to isotropic TPMS frameworks [64]. Computational Fluid Dynamics calculations on varied cell size primitive TPMS structures have been shown to increase effective thermal conductivity and improve melting behaviour under directional heat flux [63]. Gradient-designed TPMS composite PCMs analysed both numerically and experimentally [65] revealed that radial porosity gradients significantly modified heat transfer paths and improved thermal storage performance. Experimental and numerical assessments of additively manufactured TPMS–PCM composites have confirmed consistent heat transfer improvements and reduced phase-change durations [66]. While these works collectively underscore the influence of structure on PCM performance, a systematic focus on *anisotropic effective conductivity* via controlled geometric rescaling under both steady and transient conditions is still lacking.

Various material combinations are examined to evaluate TPMS skeleton impact on fully metallic and hybrid C-PCMs. Sn is chosen as inorganic filling, while the class of organic PCMs is represented by paraffin.

For the TPMS structures, an Al-Si-based alloy (Si is demonstrated to not modify the immiscible nature of the binary Al—Sn system [67]) is preferred to copper, due to low density, cost-effectiveness, and printability.

The organization of the paper is as follows. Section 2 describes the materials and numerical methods employed in the study, specifically the geometry, imposed boundary conditions, and thermophysical properties. The described approach takes inspiration from the numerical simulation adopted in [68]. Section 3 collects the results and analysis of the numerical study. Section 4 reports the conclusions and the perspectives for future investigations.

2. Materials and methods

This study is based on a program of thermal finite element analyses[1] conducted to evaluate the components of the effective thermal conductivity tensor of a TPMS hybrid/metallic composite. The thermal conductivity here referred to is the equivalent property of the composite, seen as a homogeneous continuum, expressed as a function of the microstructural features of the TPMS metallic skeleton (i.e., the porosity ε, which defines the portion of the volume occupied by PCM, in turn organic and Sn) and of a purely geometric level of rescaling. No mechanics is involved in the study.

In the following, the TPMS structures will be identified by the initial of their name, i.e., P (Primitive-Schwarz), G (Gyroid), D (Diamond), and I (I-wrapped-package graph).

The diagonal components of the effective thermal conductivity tensor are determined by solving numerically the heat conduction equation. In a 3D orthonormal reference system $\{x_i, i = 1, 2, 3\}$, according to the Fourier theory, the heat flux q_i [W/m^2] of the i-th direction is related to the temperature gradient ∇T_j [K/m] applied along j-th direction through the thermal conductivity tensor k_{ij} as

$$q_i = k_{ij} \nabla T_j \tag{1}$$

The values of the components of the thermal conductivity tensor follow from the thermal properties of the material, defined by the embedded micro-structure [69–71]. Specifically, in composites the conductivity depends on the structure of the lattice [72] and on the arrangement of the material phases [73]. For the TPMS structures here considered, the spatial disposition of lattice and materials determines symmetry axes in three orthogonal directions (i.e., the principal directions of material symmetry). The structures are isotropic in the original configuration from thermal points of view. In a thermally isotropic composite, the off-diagonal components of the conductivity tensor are zero [52]. Note that thermal symmetries might be compromised by large angular transformation, such torsion or shear, which transform the original shape of the structure, making it anisotropic. However, the focus of this study is on the effect of a unidirectional scaling applied in the direction of the principal axes of symmetry of the structure. Such transformation preserves the orientation of the principal directions of symmetry while make the lattice thermally orthotropic (or transversally isotropic). Because of the preservation of the principal symmetry axis, the present calculations are confined to the analysis of the diagonal components of the thermal conductivity tensor of the TPMS structures [71], whose components are defined in the principal symmetry reference system. By imposing a one-directional temperature gradient along one of the principal symmetry directions, the heat conduction equation is solved with finite elements, which provides the total collinear flux. The component of the effective thermal conductivity tensor in the direction of the heat flux is computed from Eq. (1), considering the equivalent homogeneous one-dimensional problem. The considered heat flux for the effective thermal conductivity evaluation is calculated as the average of the surface at lower temperature, perpendicular to the temperature gradient application direction.

The impact of the anisotropic rescaling is also evaluated under transient regime, in order to evaluate the effects of modified thermal conductivity tensor on the C-PCM thermal response, in simulated service conditions, in particular under linear temperature and constant heat flux regimes. Differently from the previous case, time-dependent Laplace equation physically describes the problem.

$$\rho_\lambda C_{p,\lambda} \frac{\partial T_\lambda}{\partial t} - k_\lambda \nabla^2 T_\lambda = 0 \tag{2}$$

ρ_λ [kg m^{-3}], $C_{p,\lambda}$ [J kg^{-1} K^{-1}] and k_λ [W m^{-1} K^{-1}] represent density, specific heat at constant pressure and thermal conductivity of the λ-th phase. In the case of the transient regime, the total PCM melting time and average temperature difference between the two domains of the composite are considered.

It is worth mentioning that the potential effect of the natural convection is here neglected, being out of the scope of the paper. This work focuses exclusively on the effect of geometric rescaling on the effective thermal conductivity, whose impact may be partially mitigated by the onset of convection. Nevertheless, it is worth noting that the proposed structures exhibit characteristic geometrical features that remain below the critical length estimated through the evaluation of the Rayleigh–Darcy parameter for the onset of convection [74].

---

[1] COMSOL multiphysics software, version 6.1 (www.comsol.com).

The consistency of the proposed model is assessed by comparing the results obtained from its application with those reported in [30,63], with particular reference to the steady-state analyses. Furthermore, the total PCM melting time predicted by the transient model is compared with the numerically derived results reported in [30]. The result of the analyses is collected in Appendix A.

2.1. Geometry

Digitalized TPMS structures are generated according to their original geometry and discretized into finite elements with the open-source software MS Lattice [75], see Fig. 2, together with the x, y and z (vertical) directions. The software allows the design of the P, G, D and IWP types of TPMS skeletons. For all these structures, developed in cubes in the non-stretched forms, cell size length L of 5 mm was selected. The cell size has been identified considering the limits of additive manufacturing printability discussed by the authors in a previous work [31]. TPMS structures with relative density $\overline{\rho}$ of 0.1, 0.2 and 0.3, coinciding with high porosity, $\varepsilon = \overline{\rho} - 1$, were considered.

The structures have been generated varying the density of points per unit cell n from 50 to 400. As n increases, the accuracy of the representation of TPMS surfaces increases as well. The higher value of $n = 400$ was then used for all cell types and porosity values. Structures produced with MS Lattice have been saved in electronic format (.stl) and directly imported in COMSOL software.

As shown in Fig. 2a, the composite unit cubic cell was obtained by merging the TPMS skeleton with the complementary volume of the cube, occupied by the PCM material and split in 2 disjointed domains. The skeleton was made of AlSi10Mg alloy material, whereas the surrounding volumes are both filled alternatively with one of the two investigated phases, i.e., Sn or C80 paraffin. Each structure is thus characterized by skeleton type and porosity, which defines the amount of PCM.

The original geometry of each TPMS structure was discretized in COMSOL and subsequently modified by applying a rescaling only in the z direction defined by the scaling ratio N

$$N = \frac{l_z}{L_z} \tag{3}$$

where l_z is the modified length of the skeleton lattice along z (Fig. 2b). The scaling operation, directly performed in the software, allows to achieve the expansion of the structure in the z direction up to 5 times, i.e., $N = 5$, starting from $N = 1$ (unscaled structure) with a $N = 1$ step. This operation, performed considering the central point of the structure as the scaling center, allows to maintain the same volume fraction between the phases of the composite. While the rescaling in z introduces potentially anisotropic conductive properties in lattices that are characterized by two interconnected volumes disjoined by a thin metal skeleton, it clearly destroys the ubiquitous zero mean curvature characteristic of TPMS lattices. For this reason, in the following, geometries are referred to as 'rescaled P, G, D, and IWP lattice'.

Thermal conductivity tensor components are evaluated on single cells with the means of steady-state analyses, whereas vertical arrangement of stacked cells is employed for comparing the transient behaviour of the resulting C-PCMs. In particular, for this latter case study, four stacked cells having $N = 1$, two with $N = 2$ and one $N = 4$ are designed and tested in the same conditions in order to evaluate transient regime effects. The structures are chosen having the same height along z-axis and, consequently, giving comparable results.

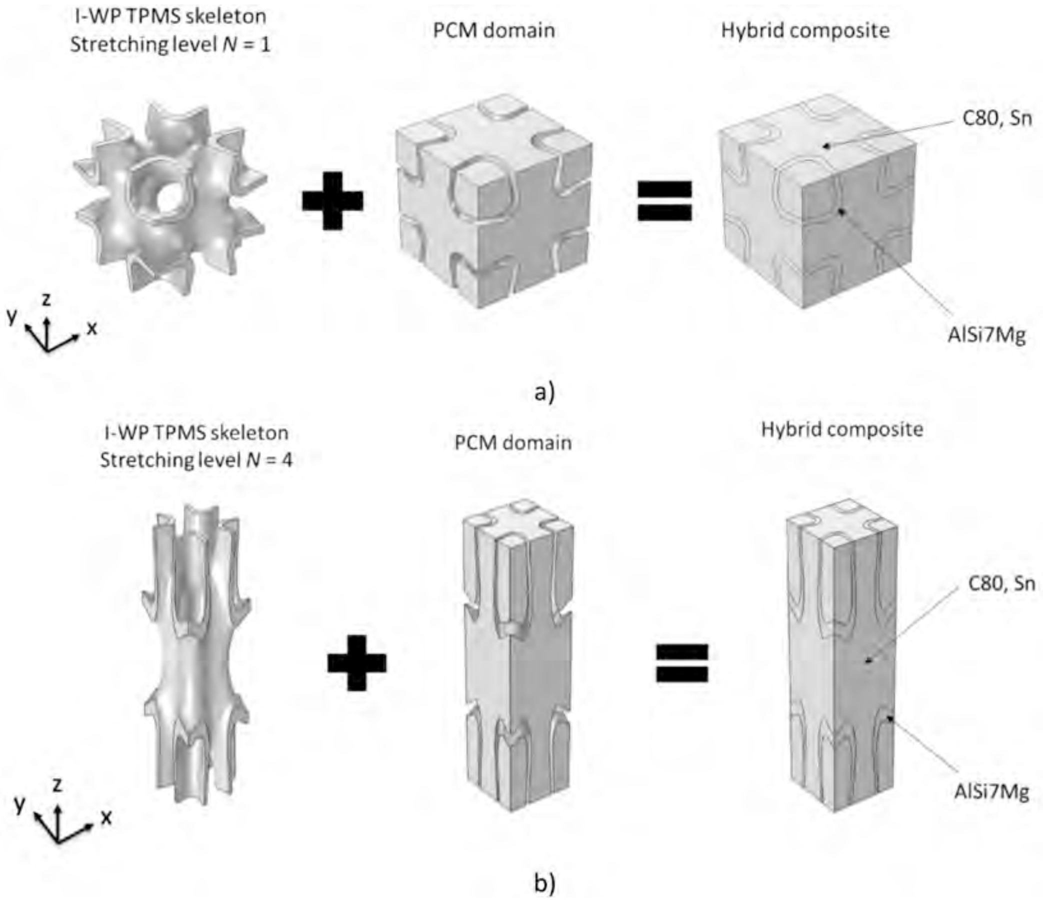

Fig. 2. Hybrid composite. Visualization of the geometry, consisting of a tripy periodical minimal surface (TPMS) metal skeleton and of a phase changing material filling (PCM). (a) Original state, $N = 1$; (b) rescaling in z direction, $N = 4$.

2.2. Thermophysical properties of the lattice skeletons and filling materials

The material chosen for the TPMS lattices is a metallic alloy, AlSi7Mg, because it is suitable for Powder Bed Laser Fusion (PBLF) manufacturing technique. Additionally, the alloy combines high thermal conductivity and low density, which are appealing properties in view of practical applications [76]. The AlSi7Mg thermophysical properties used in the present simulations have been taken from experimental characterizations reported in the literature [77,78], and are assumed to be temperature independent for the steady-state thermal conductivity estimation, in consideration of the reduced range of temperature used in the simulations, i.e., from RT (25 °C) to RT + 1 °C. Also the thermophysical properties of the filling materials, i.e., organic PCM and Sn, have been taken from the literature [78,79]. The choice of the filling materials is based on their potential applications in thermal energy management systems. Due to its high latent heat of fusion per unit mass, inexpensiveness, and large availability, the commercial C80 paraffin has been chosen as representative of the class of organic PCMs. The thermophysical properties of Sn have been estimated from porosity dependence models gathered from literature [80]. The properties used in this steady-state study are collected in Table 2. The selection of different PCMs can be relevant for applications such as power modules operating at multiple temperature levels, where the transition temperatures of the adopted materials can be effectively exploited [81,82].

On the other hand, a wider temperature range is explored in the transient simulations. In this case, the study of the Sn-based C-PCM is neglected and only the AlSi7Mg and C80 combination is considered due to the higher benefits offered in heat conduction with respect to the fully metallic composite. The temperature dependence of thermophysical properties is taken into account for AlSi7Mg skeleton [77,78], whereas C80 properties dependence is neglected, due to their slight changes in the temperature range of interest with respect to the AlSi7Mg ones. Its thermophysical properties in the liquid state are modelled on the bases of the models proposed by Li et al. [80], as well as the transition temperature range (348–358 K) and the related latent heat (235,000 J kg^{-1}). The melted fraction of the PCM phase is assumed to be linearly dependent on the temperature.

2.3. Boundary conditions for steady state and transient analyses

As previously said, for the assessment of the conductive properties of the C-PCM composites heat conduction steady-state analyses have been conducted. To evaluate the three diagonal components of the effective thermal conductivity tensor, the same set of boundary conditions suitably rotated is applied in turn to the three i-directions, see Fig. 3. Ideal thermal continuity is assumed on the interfaces between the two phases of the composites. However, it is worth mentioning that interface mechanisms may affect the efficiency of thermal transport between the two phases of the composite [83]. Four external surfaces, in parallel pairs, are thermally insulated, i.e., no thermal flux is allowed, while on the remaining two parallel surfaces a unidirectional positive temperature difference ΔT_i of 1 °C is applied, by assigning the room temperature RT on one surface and the $RT + \Delta T_i$ temperature on the parallel surface.

Transient regime analyses have been conducted only for the cases of C-PCMs, where the TPMS AlSi7Mg alloy skeleton is filled with the C80 paraffin wax. The analyses are limited to the low-temperature PCM, namely paraffin wax, since previous studies have shown that the thermal conductivity enhancement is relatively limited. More significant effects are instead expected for the organic PCM. In fact, for the heating phase of the thermal cycle here investigated, the low thermal conductivity and diffusivity of the PCM phase of these composites may play a relevant role in the thermal energy storage. Fig. 4 shows the selected boundary conditions applied. As a representative example, only the four-time rescaled structure is here presented for the two proposed case studies. The ideal thermal continuity hypothesis still holds among the various interfaces of the composite. In this case all the surfaces of the resulting structures are considered as adiabatic, whereas the heat source (either linear temperature ramp with 100 K h^{-1} slope, Fig. 4a, simply named as T condition, or constant heat flux of 1850 W m^{-2}, Fig. 4b, HF condition) is applied at the bottom surface of the C-PCM, perpendicular to the rescaling direction.

Table 2
Thermophysical properties of AlSi7Mg, assigned to all the studied TPMS skeletons, C80 paraffin and Sn, related to the PCM filling material in the composite.

	AlSi7Mg	C80	Sn
Thermal conductivity, k [W m^{-1} K^{-1}]	185	0.45	63.9
Specific heat, C_p [J kg^{-1} K^{-1}]	920	2300	228
Density, ρ [kg/m^3]	2700	810	7311

The HF condition was selected based on the average heat absorbed within the unstretched C-PCM under the temperature ramp condition T, a condition previously adopted by part of the authors in an earlier work [84].

The initial temperature of the composite structures was homogeneous, at 25 °C. These values have been selected following what done in a previous paper related to various features of cubic cells (i.e. with $N = 1$) in which the effect of cell-size was considered (5 mm) [31]. Specifically, the constant heat flux value corresponds to the average heat flux obtained for unscaled structure in the case of the linear temperature ramp for the investigated lattice size and porosity of 0.8 [84].

Transient regime numerical simulations were conducted to reach the melting of the organic PCM by imposing a temperature raise to surpass the composite transition temperature. For these analyses, the geometrical samples have been designed to have the same height.

2.4. Meshing and FEM simulations

The meshing step was then performed in MS Lattice, using tetrahedral quadratic elements. Automatic meshing was then applied, considering the maximum element size h as meshing parameter.

The steady-state solution of the heat conduction problem provides the distribution of the temperatures within the domain and of the heat flux on the two surfaces with imposed temperature. The integral of the flux on the lower temperature surface defines the total flux, used to compute the conductivity tensor component from Eq. (1).

Mesh sensitivity analysis was carried out for the unscaled P structure with 0.8 porosity filled by paraffin, the material with the highest difference of thermal conductivity with respect to the Al-alloy. In these cubic structures, the effective thermal conductivities resulting after rescaling are the same in various directions, and they were calculated for various meshing parameters. The thermal conductivity computed for the mesh with minimum element size ($h = 0.0203$) was taken as reference to compute the relative errors. Results are presented in Table 3.

The previous studies have shown that the effective thermal conductivity values of TPMS are independent on the discretization size in the selected meshing parameters. The maximum element size of 0.0558 was selected this situation, corresponding to 964,106 elements per unit cell, reaching an error of 0.0157% with respect to the finest mesh. The same maximum size was considered for other composites.

The same mesh is adopted also for the transient regime simulations. In this case, a further time step sensitivity analysis is performed to evaluate its impact on the results. The development of PCM liquid fraction with respect to the simulation time is taken as the reference physical quantity. The preliminary analysis suggests 0.1 s as the proper time step for performing the numerical simulations.

3. Results and discussion

This section presents and discusses the results of the numerical simulations. First, the results of the effective thermal conductivity,

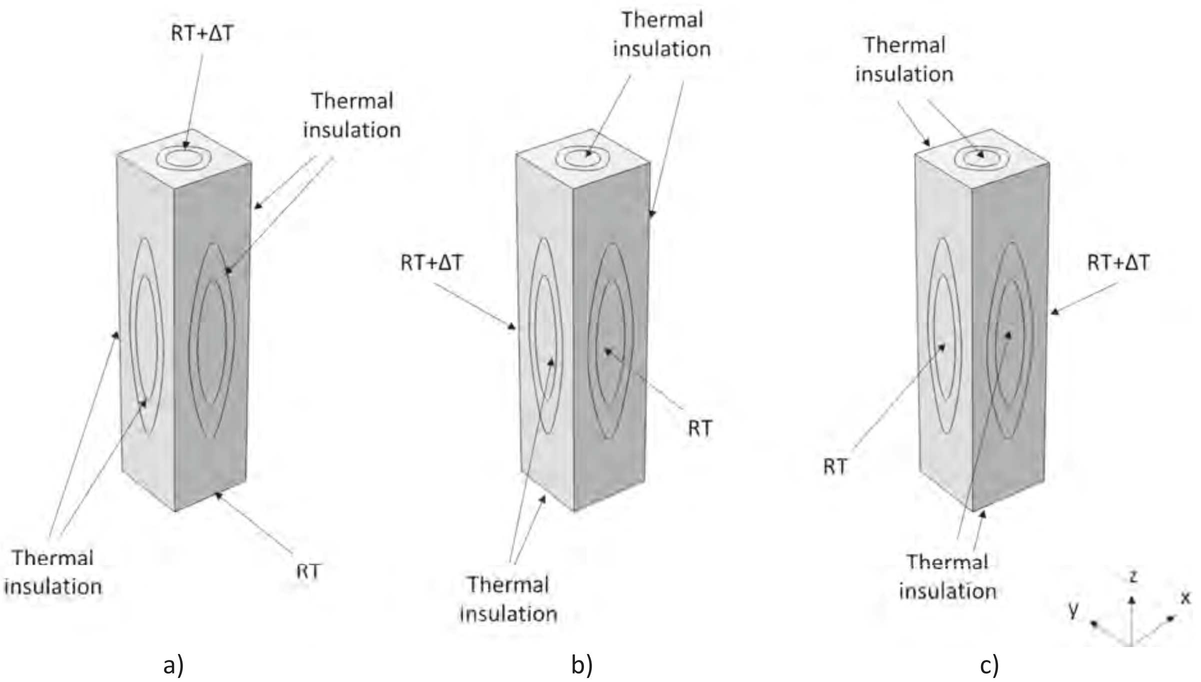

Fig. 3. Boundary conditions scheme for the calculation of the composite effective thermal conductivity tensor diagonal components along: (a) z direction; (b) y direction; (c) x direction.

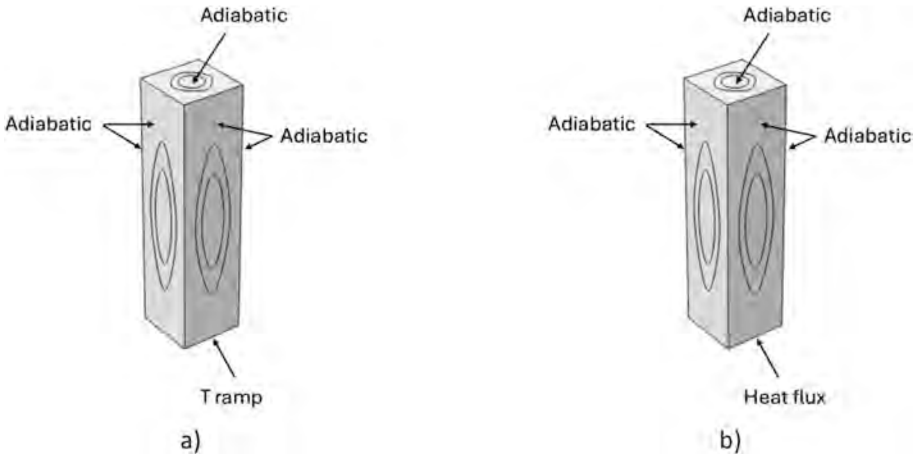

Fig. 4. Transient regime boundary conditions for C-PCM thermal response evaluation under: (a) linear temperature ramp (T condition) and (b) constant heat flux (HF condition).

Table 3
Effective thermal conductivity calculated for the cubic P structure with porosity 0.8 made of AlSi10Mg alloy filled by C80 paraffin with various meshing parameters. The selected maximum element size and corresponding data are in italics.

Maximum element size h [mm]	Number of elements per unit cell	$k_{eff,\ z}$ [Wm^{-1} K^{-1}]	Relative error (%)
0.3040	43,690	25.555	0.0626
0.1930	58,233	25.553	0.0548
0.1520	85,072	25.552	0.0509
0.1010	191,870	25.550	0.0431
0.0812	347,839	25.547	0.0313
0.0558	964,106	25.543	0.0157
0.0355	1105,616	25.542	0.0117
0.0203	2,047,537	25.539	–

derived from the steady-state analyses are presented, followed by a subchapter involving the results of the transient regime analyses.

3.1. Steady-state analyses

The components of the effective thermal conductivity tensor are evaluated by varying both the level of skeleton rescaling through the parameter *N* and the initial porosity of the composite. The incidence of rescaling level N, skeleton architecture type, and structure porosity on the diagonal components of the effective thermal conductivity tensor is rendered in terms of analytical expressions of functions that best fit the numerical results.

To facilitate the comparison among materials characterized by different values of thermal conductivity, numerical results are hereafter reported in terms of dimensionless indexes that can be easily calculated from the upper and lower Wiener bounds, i.e., the theoretical maximum and minimum values, $k_{\parallel}$ and $k_{\perp}$, respectively. For a composite made of two phases, where the thermal conductivity of the inclusion is k_1 and the thermal conductivity of the matrix is k_2, the bounds $k_{\parallel}$ and $k_{\perp}$ are defined as:

$$k_{\parallel} = k_1\varepsilon + k_2(1-\varepsilon) \tag{4}$$

$$k_{\perp} = \left(\frac{1-\varepsilon}{k_1} + \frac{\varepsilon}{k_2}\right)^{-1} \tag{5}$$

Note that $k_{\parallel}$ and $k_{\perp}$ are only related to thermal conductivity and porosity (thus to the volume fraction) of the phases, they are equal in all directions and unaffected by rescaling levels.

The first dimensionless index here introduced, η_i, is referred to as microstructural efficiency in the i-direction:

$$\eta_i = \frac{k_{eff,i}}{k_{\parallel}} \tag{6}$$

where $k_{eff,i}$ is the effective thermal conductivity of the composite [$\mathrm{Wm^{-1}\ K^{-1}}$] calculated referred to the i-th direction. It should be noted that, in this study, the microstructural index η_i has been defined differently from what was originally proposed by Rawson et al. [85] for a generic lattice composite, where a unique value of microstructural efficiency, calculated as the ratio between the effective isotropic conductivity (i.e., the trace of the conductivity tensor divided by the dimensionality) and $k_{\parallel}$ was considered [85,86]. Only when thermal isotropic lattices are considered along their principal directions, η_i is equal in the three directions and recovers the index η proposed in [85]; while in a non-isotropic structure, indexes η_i are direction dependent. This observation is useful to estimate the effects induced by geometry changes in the rescaling direction.

The second dimensionless index is the morphological index μ_i in the i-direction, defined as

$$\mu_i = \frac{k_{eff,i} - k_{\parallel}}{k_{\parallel} - k_{\perp}}. \tag{7}$$

μ_i measures the relative distance of the effective thermal conductivity from the theoretical maximum and minimum values. The index, introduced as a unique value for isotropic structures in [86], for the anisotropic structures considered here assumes different values in the three principal directions. The index is useful to estimate the effects induced by geometrical changes performed in the rescaling direction along a generic principal direction.

It has been observed elsewhere [85,86] that the effective thermal conductivity can be approximated as the product of the thermal conductivity of a representative phase (often the matrix, k_2) and of a correction term which is function of: (i) the geometry distribution of phases; (2) the heat flow direction; and (iii) of the thermal conductivity ratio r, defined as

$$r = \frac{k_1}{k_2}, \tag{8}$$

where subscript 1 refers to the inclusion and subscript 2 to the matrix phase. On the other hand, the indices η_i and μ_i are related to thermal conductivity ratio r, geometry, and flow direction. It follows that these indexes are more general and can be extended to all composites characterized by the same r [86]. For this reason, hereafter results are presented in terms of η_i and μ_i rather than in terms of $k_{eff,i}$.

Note that, for the cases analysed in the present study, the matrix phase (subscript 2) corresponds to the AlSi10Mg skeleton and the inclusion (subscript 1) corresponds to the PCM phase, in turn C80 or Sn. Specifically, the r value for the composite Al—Sn is 0.35, and that of the composite Al—C80 is roughly two orders of magnitude smaller, $0.25 \bullet 10^{-2}$. While the first composite is representative of situations where a skeleton is combined with a slightly less conductive medium, the second composite is representative of conditions where the filling phase is very low conductive. Interestingly, Al—C80 can well represent the cases Al-air and Al-water, which exhibit r values of $0.14 \bullet 10^{-3}$ and $0.91 \bullet 10^{-2}$, respectively.

Here The results obtained in this work are in agreement with those reported by Qureshi et al. [30]. These authors numerically tested the effective thermal conductivity for P, G and I-based C-PCMs made up by AlSi10Mg and paraffin. Although slightly lower, possibly due to the lower thermal conductivity of AlSi10Mg with respect to AlSi7Mg (175 $\mathrm{W\ m^{-1}\ K^{-1}}$ vs 185 $\mathrm{W\ m^{-1}\ K^{-1}}$), their results are in the same order of magnitude of this paper. The authors report indeed 11.70, 11.16 and 10.54 $\mathrm{W\ m^{-1}\ K^{-1}}$ for P, I and G with $\varepsilon = 0.9$, respectively. The results of the present paper on the other hand give 12.87, 12.13 and 11.87 $\mathrm{W\ m^{-1}\ K^{-1}}$ for P, I, G-based AlSi7Mg-Sn combination.

3.1.1. *Effect of the rescaling level*

For a lattice with initial porosity $\varepsilon = 0.8$ and a rescaling in the z direction, Fig. 5 shows, in terms of microstructural efficiency, the dependence of the effective thermal conductivity k_{eff} in x, y and z directions with respect to the rescaling level. In the diagram, the effective thermal conductivity in the rescaling direction, $k_{eff,z}$, is identified by full symbols of different colour according to the cell type before rescaling. Hollow symbols identify the effective thermal conductivity in the remaining two directions, $k_{eff,x}$ and $k_{eff,y}$.

For easiness of representation, the symbols in the diagrams are referred to with a symbol (P, G, D, I, related to the original, un-scaled TPMS skeleton), followed by a number (denoting the rescaling level N), and by an orientation x, y and z (denoting the direction of the C-PCM k_{eff} tensor). Note that, with the exception of G, in all structures the values of $k_{eff,x}$ and $k_{eff,y}$ coincide, due to the symmetries of the composites [87]. Fig. 5 clearly shows that geometric rescaling induces a strong anisotropy in the effective thermal conductivity tensor. The diagrams confirm the effectiveness of the skeleton rescaling operations in modifying $k_{eff,i}$ along x, y and z, that are all equal when no rescaling is applied. In particular, $k_{eff,z}$ exhibits a marked increase with N for small values of the rescaling level, reaching a plateau at higher values of N. The opposite trend is observed for $k_{eff,x}$ and $k_{eff,y}$, revealing a strong anisotropy of the effective thermal conductivity. The comparison between results for the two C-PCMs (Fig. 4a and b) shows that the change in microstructural efficiency for a selected original C-PCM composite is related not only to the rescaling of its geometry along z direction, but also to its thermal conductivity ratio. The combined role played by rescaling and relative thermal conductivity of the composite phases has been mentioned in literature in works focusing on the effective thermal conductivity of composites containing fibers, modelled as rotational ellipsoids, whose geometry resembles a sphere rescaled in the fiber direction [88–92].

Fig. 6a–b shows the η difference, i.e., the percentage relative incremental gain of microstructural efficiency between two nearest rescaling levels. In the sets of simulations performed here, the most consistent incremental gain of effective thermal conductivity in z direction for a rescaling along the same direction has been reached for a rescaling level $N = 2$ with respect to $N = 1$. Under these conditions, for the composite with Sn as filling phase (Fig. 6b), the increase of η in z direction is not affected by rescaling in z direction as it happens for the other filling material (C80 paraffin, Fig. 6b) with far lower thermal conductivity relative to the skeleton. For both composites, when the rescaling in z direction is larger than 5, no further significant benefit to η difference in z direction is observed. Thus $N = 5$ defines an upper-bound for modification to the lattice geometry in view of achieving a higher effective thermal conductivity along the rescaling direction. Finally, the comparison between the microstructural indexes (Fig. 5a–b) and the related percentage differences (Fig. 6a–b) clearly shows that the lattice cell rescaling along the z direction (for higher N) gives a marked advantage in the rescaling direction only for composites characterized by a thermal

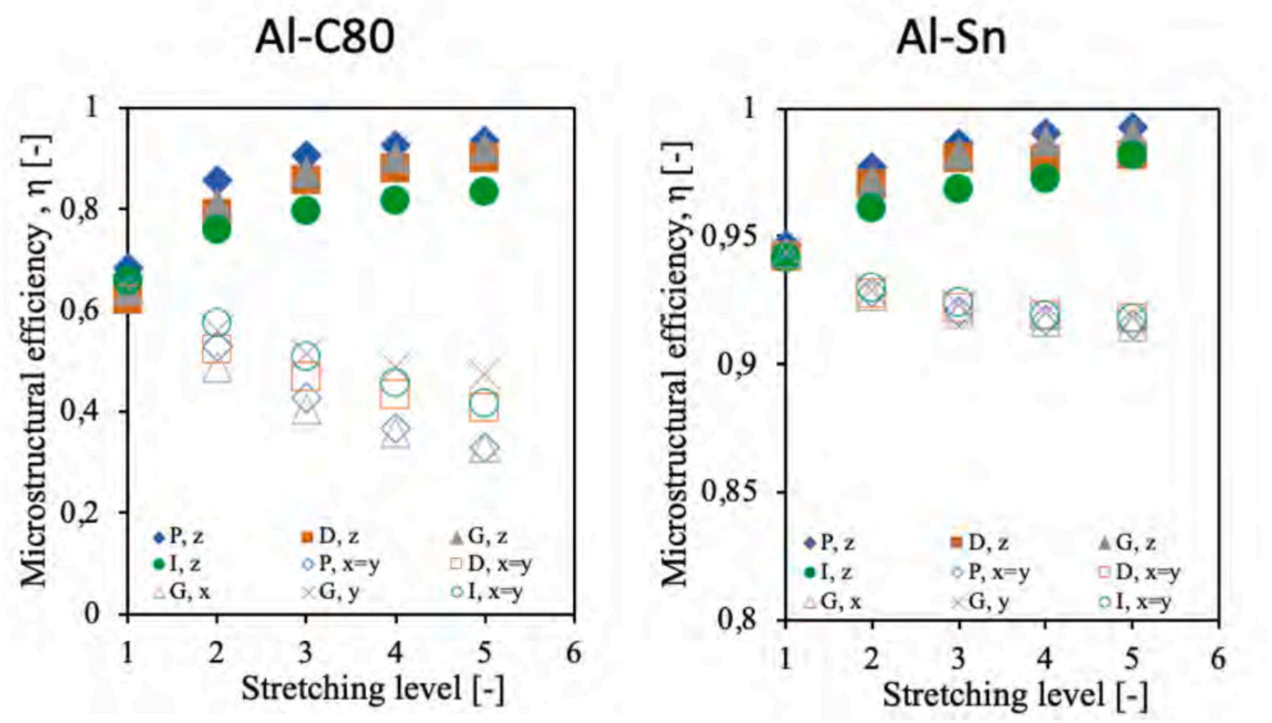

(a) (b)

Fig. 5. Analysis of the effect of the rescaling level N on the effective thermal conductivity along z (full symbols), y and x (hollow symbols) in terms of microstructural efficiency: (a) Al-C80 composite; (b) Al-Sn composite. Note that the microstructural efficiency scale is different in the two graphs.

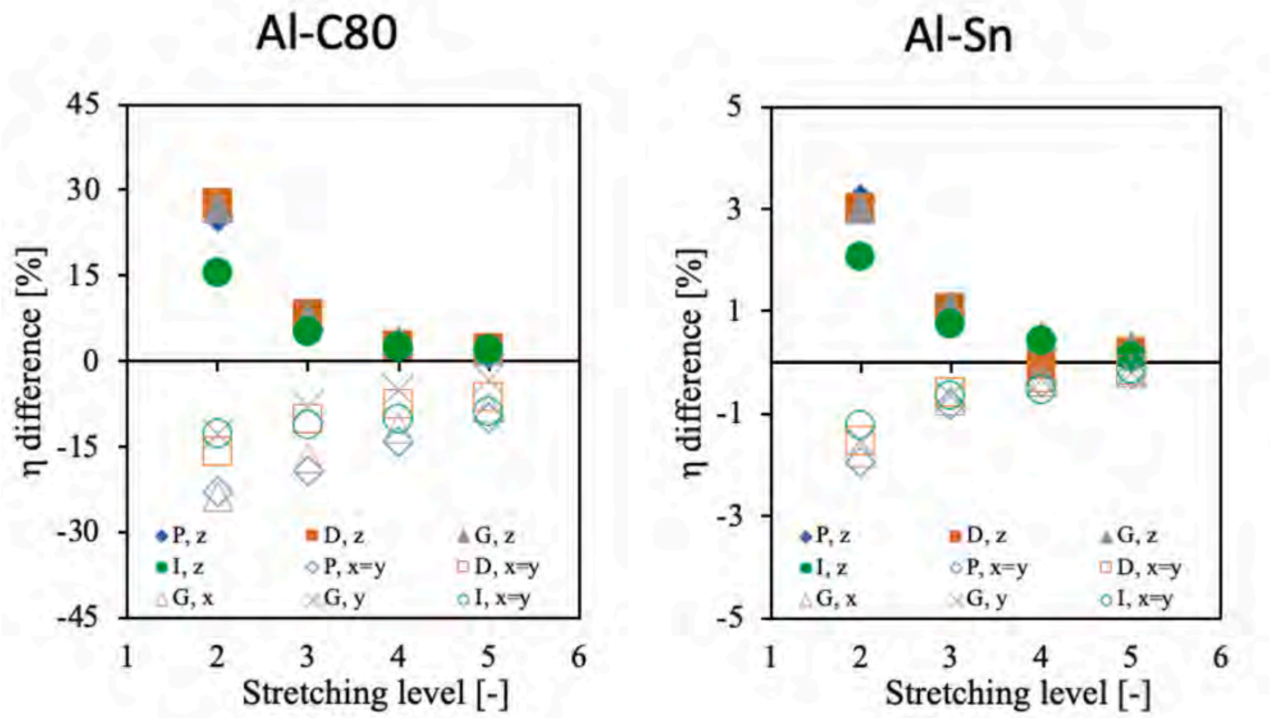

(a) (b)

Fig. 6. Analysis of the effect of the rescaling level N on the components the effective thermal conductivity along z (full symbols), y and x (hollow symbols). Percentage of the incremental gain of the microstructural efficiency η between two values of N. (a) Al-C80 composite; (b) Al-Sn composite. It is worth mentioning that different y-scales are adopted for the materials.

conductivity of the filling material far lower than that of the skeleton (Al-alloy in the present case). Furthermore, Fig. 6a–b shows that the incremental gain in microstructural efficiency η is lower when it is calculated for x and y directions, with no significant difference for rescaled P, D and I structure type.

Figs. 5–6 indicate that the phase arrangement P is the most efficient in terms of η for highly conductive composites, while I-WP (I in the figures) is the phase arrangement getting less advantage from geometric rescaling. This behaviour can be explained by the geometric arrangement of the PCM domains in the I-WP structure. The geometric rescaling determines the presence of extended interconnected portions of organic PCM, which remains almost normal to the heat flux when the rescaling level N in z direction is increased from 1 to higher values.

The same analyses performed for other two values of porosity ($\varepsilon = 0.7$ and $\varepsilon = 0.9$) provided very similar results, which are omitted here for the sake of conciseness.

The availability of the microstructural efficiency index η in various directions is useful for practical applications, since it allows to calculate the effective thermal conductivity for a desired porosity from the theoretical maximum, which is not affected by the rescaling of the cell in various direction. Tables A1 to A2 (Appendix A) collect analytical fitting equations, for the Al—C80 and Al—Sn cases, in the investigated ranges of porosity ($0.7 \leq \varepsilon \leq 0.9$) and scaling ratio in z direction ($1 \leq N \leq 5$). Analytical equations can be useful for estimating the effective thermal conductivity k_{eff} of composites made by different materials but with absolute thermal conductivity in the range of the ones considered in this study. For example, the k_{eff} of Al-water or Al-air composites, which have important applications in heat exchangers, can be easily derived from the case Al—C80, since the organic PCM thermal conductivity is close to that of water and air. The proposed analytical equations can be extended to composites characterized by the same arrangements and composed of materials exhibiting similar thermal conductivity ratios, particularly in applications where heat must be effectively guided away from large components, for instance.

The morphological index μ calculated in x, y and z directions for composite structures characterized by $\varepsilon = 0.8$ are shown in Fig. 7a–b for Al—C80 and Al—Sn composite, respectively. Results or the two composites are very similar, and it can be concluded that, for the values of porosity investigated here, μ is almost independent of r. This confirms also for rescaled structures what has been previously observed for TPMS composite [86]. Analytical expressions of the fitting curves of morphological indexes in x, y and z directions, for composites rescaled in z direction, have been derived and are listed in Tables A3 and A4 (Appendix A).

3.1.2. Effect of the porosity

The dependency of microstructural and morphological indexes in x, y and z directions on porosity shows similar trends for all the rescaled structures. Results are here shown in Figs. 8–9 only for the representative C-PCMs based on P structure. In these diagrams full symbols refer to the principal component of the effective conductivity tensor $k_{eff,z}$ in direction z, hollow symbols refer to the other principal components of the effective conductivity tensor; symbol colours differ according to the rescaling level N.

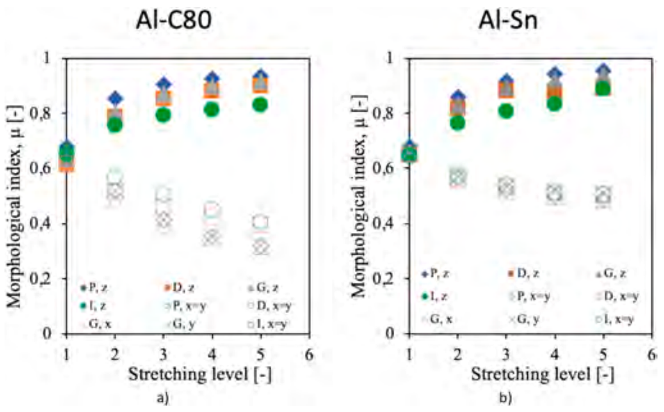

Fig. 7. Analysis of the rescaling magnitude N ($1 < N < 5$) impact for Al-C80 composite (6a) and for the Al-Sn composite (6b) on the morphological indexes along z (full symbols), y and x (hollow symbols). In both cases a reference porosity of 0.8 was selected.

The comparison between Fig. 8a and b, showing microstructural efficiency of the C-PCMs built with different filling PCMS, reveal that the effect of the porosity on efficiency index depends both on geometry rescaling and composition of the material. Specifically, for higher rescaling levels the effect of higher porosity is less relevant on $k_{eff,z}$, more relevant on $k_{eff,x}$ and $k_{eff,y}$. Furthermore, for Al—C80 C-PCMs, thermal efficiency in x and y directions slightly decrease with increasing ε (Fig. 8a), while for Al—Sn C-PCMs the same index clearly increases with increasing ε (Fig. 8b). Thus, also when porosity-dependence is considered, the thermal conductivity ratio r between the two phases of the composite plays the main role. For a high thermally conductive phase such as Al-alloy, an organic PCM filler has a stronger influence on the effective thermal conductivity than a metal Sn filler. Analytical expressions of the fitting curves of microstructural efficiency indexes in x, y and z directions as function of the porosity, for composites rescaled in z direction, have been derived and are listed in Tables A5 and A6 (Appendix A).

The dependence of the morphological index μ on porosity, in the range $0.7 \leq \varepsilon \leq 0.9$, is shown in Fig. 9a and b for Al—C80 and Al—Sn composites, respectively. In agreement with the results of the previous section and with the literature, the morphological index is not affected by the nature of the phases of the composite in the examined porosity range. Fig. 9 shows only the P structures, but the trend is the same for other structures. For all, fitting equations of porosity-dependence of morphological index μ are given in Tables A7 and A8 (Appendix A). In general, it is worth mentioning that geometrical rescaling does not modify the original porosity (i.e., the volume ratios between the phases are constant, independently from the entity of the rescaling operations) but significantly affect the arrangement, shape, and connectivity of pores. Aligned or elongated pores with respect to the direction of temperature gradient may favour directional heat flow, thus more connected solid pathways produced by rescaling improve conductivity by providing continuous paths for heat transfer [52].

3.2. Transient regime analyses

Transient simulations were performed to evaluate how the anisotropic conductivity induced by geometric rescaling affects the thermal response of the composite PCM during melting. For transient regime analyses, same height samples made of stacked cells of equal height and different rescaling levels, i.e., 1, 2 and 4, were numerically tested under T (Fig. 10a, solid bars) or HF condition (Fig. 10a, dashed bars), using a linear ramp starting from an initial homogeneous room temperature. The main results for various simulations are summarized in Table 4 in terms of onset of melting (t_i) and complete melting time for the PCM phase (t_f).

As expected, under the T condition, the PCM at the basis of the C-PCM structure reaches the PCM melting temperature at the same time (t_i) for all the structures, thus the rescaling effect can be observed only in terms of the complete melting time (t_f) or in terms of the difference $\Delta t = t_f - t_i$, defining the duration of the PCM melting process. Under the HF condition, the melting onset time increases in all cases where the thermal conductivity is increased by the geometrical rescaling. However, it is not possible to establish a correlation between the thermal conductivity of TPMS cell and t_i. An explanation for this behaviour is that higher thermal conductivities favour an efficient heat transfer in the direction of the rescaling axis, in particular within the Al-based skeleton, reducing the heat flux reaching the inner PCM zones. Clearly, this is

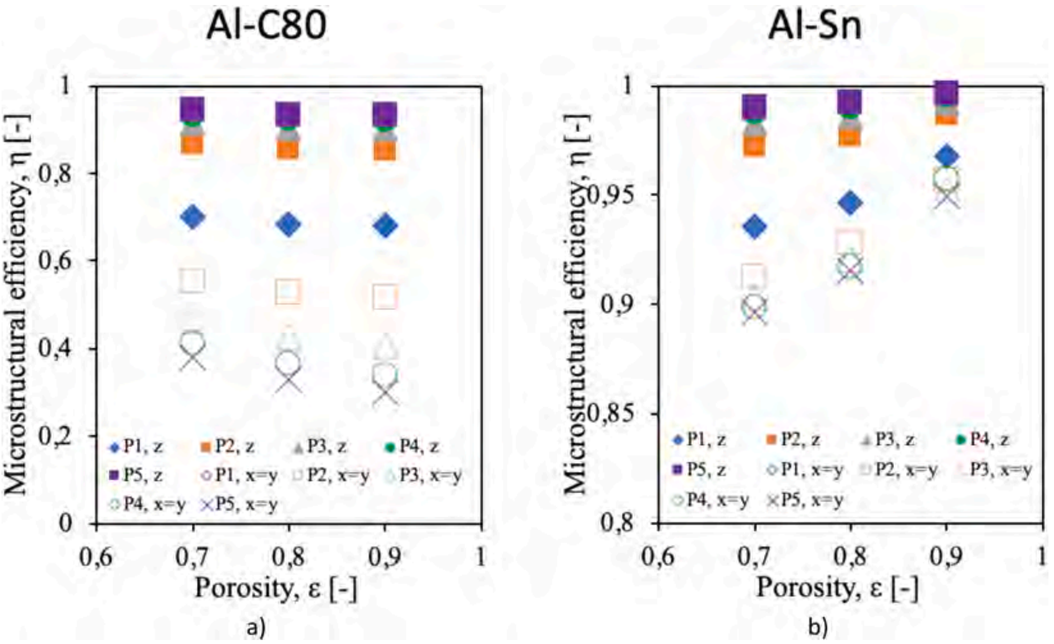

Fig. 8. Analysis of the effect of the porosity of the metallic TPMS lattice on the principal components (full symbols: z; hollow symbols: y and x) of the effective thermal conductivity tensor in terms of microstructural efficiency η. Several rescaling levels N are considered. (a) Al-C80 composite; (b) Al-Sn composite. Two different scales are adopted for the two combinations of examined materials.

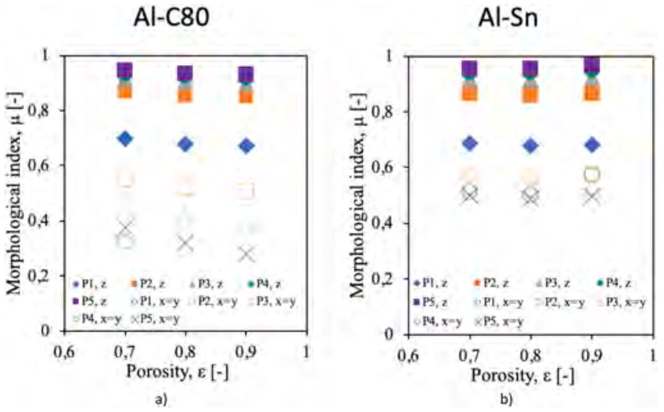

Fig. 9. Analysis of the effect of the porosity ε on the morphological efficiency (full symbols: z; hollow symbols: y and x) of the effective thermal conductivity tensor in terms of morphological index μ. (a) Al-C80 composite; (b) Al-Sn composite.

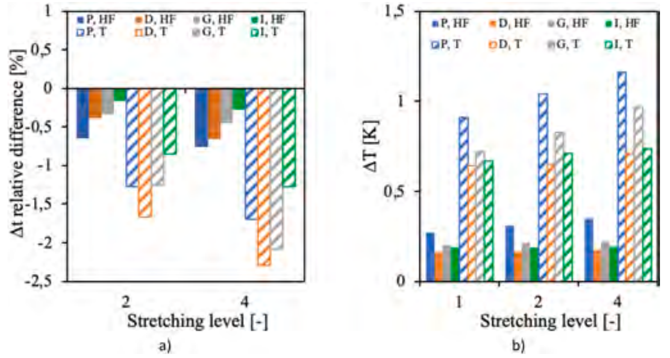

Fig. 10. (a) Time percentage difference for PCM full melting with respect to unscaled structure. (b) Index ΔT_{Al-PCM}, maximum domain average temperature difference between metallic and PCM domains. Solid bars denote T type boundary condition; dashed bars denote HF type boundary conditions.

related not only to the C-PCM thermal conductivity, but also to the arrangement of the metallic skeleton.

To visualize the effects of geometrical rescaling, in Fig. 10a is reported the difference in duration of the melting process time Δt with respect to the unscaled structures ($N = 1$). For both T and HF boundary conditions, the increment in the rescaling level causes a reduction of the time for the PCM melting, more evident and with a more marked sensitivity on the rescaling level when HF conditions are applied. For the investigated structures with the same total height, the difference in time to reach the full melting is about 1% for HF conditions and between 1 and 2.5% for T conditions. In the case of HF, this observation is consistent with the thermal conductivity trend, i.e., architectures with higher thermal conductivity exhibit faster melting, except for D and G structures that are inverted, characterized by similar thermal conductivity in all rescaling levels. The undefined trend observed for the onset of melting is confirmed for the complete melting time of PCM with respect to the unscaled structure. The diamond structure D displays the fastest PCM melting onset despite its lower thermal conductivity, suggesting that the implication of using this topology should be considered in addition to thermal conductivity in the design to match specific needs of TES/TEM structure.

The effect of the topology of the rescaled Al-based skeleton structures under different heating conditions is illustrated in Fig. 11, where only the D and P structures with the extreme behaviour are shown.

The C-PCM based on the TPMS D structure emphasize the difference in imposing HF or T boundary conditions. With respect to T conditions, HF conditions cause a slower progression of the narrow regions where PCM melting occurs, leading to a more gradual heat storage for TES/TEM structures based on these C-PCM structures [84]. The regions along z axis where PCM melting occurs are clearly visible for the case $N = 1$ in the D structure, characterized by a smaller size of the PCM regions and by a relatively homogeneous temperature distribution within each of them. Even though constructed by stacking 4 unit cells, the P structure is coarser than the D structure. The P topology, while improving thermal conductivity and widening the size of the melting regions along the z axis, in PCM regions favours temperature and liquid volume fractions

Table 4

Summary of simulation results in terms of times for onset (t_i) and completion (t_f) and of their difference of PCM melting time for investigated TPMS structures (P,D,G,I), rescaling levels (N = 1,2,4) and heating conditions (T or HF).

HF condition	t_i [s]				t_i [s]				$t_f - t_i$ [s]			
N↓ cell type→	P	D	G	I	P	D	G	I	P	D	G	I
1	1310	1298	1302	1300	3160	3108	3099	3110	1850	1810	1797	1810
2	1317	1310	1310	1306	3155	3113	3101	3113	1838	1803	1791	1807
4	1320	1313	1312	1309	3156	3111	3101	3114	1836	1798	1789	1805

T condition	t_i [s]				t_i [s]				$t_f - t_i$ [s]			
N↓ cell type→	P	D	G	I	P	D	G	I	P	D	G	I
1	1800	1800	1800	1800	2270	2280	2280	2270	470	480	480	470
2	1800	1800	1800	1800	2264	2272	2274	2266	464	472	474	466
4	1800	1800	1800	1800	2262	2269	2270	2264	462	469	470	464

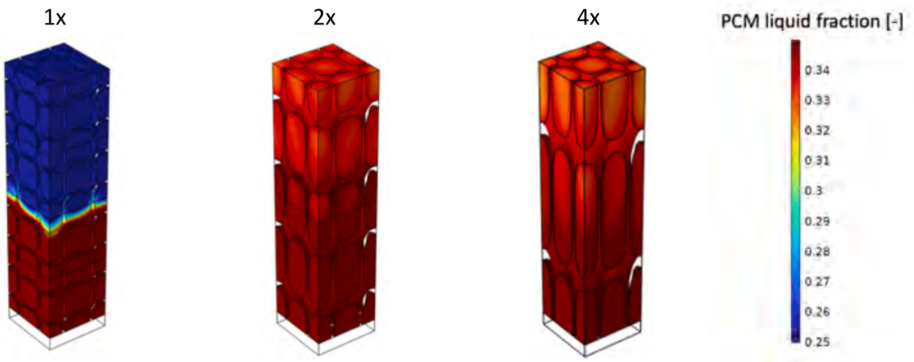

a) D structure, HF conditions

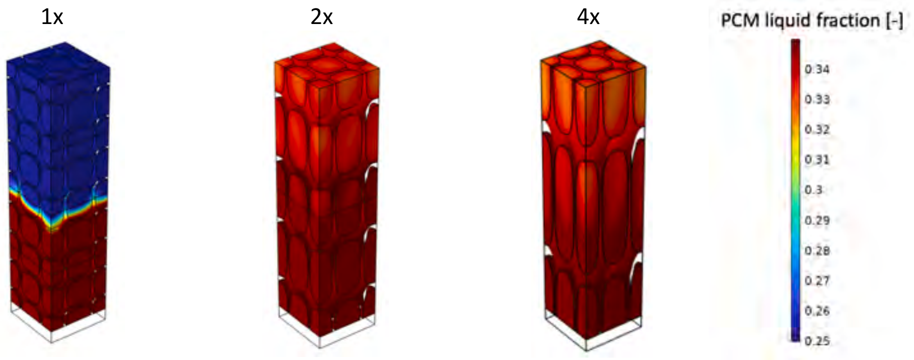

b) D Structure, T condition

Fig. 11. PCM liquid fraction distribution at the final time (2000 s) of the transient simulation, for rescaling levels 1×, 2× and 4×.

inhomogeneity.

Geometrical rescaling has a double effect on the distribution of temperature and volume fraction. The increased thermal conductivity widens the regions within which PCM melting occurs. At the same time, rescaling increases the distance between the Al skeleton and the core of massive PCM regions, growing the inhomogeneity in the distribution of liquid volume fraction when in the melting temperature range, effect clearly visible, for example, by comparing the P structure with rescaling levels 2 and 4.

The detailed analyses of volume fractions of liquid and temperature distribution within the organic PCM in D and P structures suggested the introduction of a simple index accounting for the effects of the effective thermal conductivity and volume fraction of the liquid PCM phase. The index, ΔT_{Al-PCM}, defines the maximum difference in the average temperature of the metallic and PCM domains during the PCM melting, and increases with both thermal conductivity and inhomogeneities in extended PCM regions. This index therefore provides a simple measure of the thermal homogeneity within the composite during the melting process. Its values are shown in Fig. 10b. The index reveals that the homogeneity of the thermal distribution in the C-PCM decreases as the rescaling level increases, indicating that rescaling PCM reduces the efficiency of the heat transfer needed to fill the entire domain. D structures have the best topology to lower the temperature differences (Fig. 10b). Furthermore, the index ΔT_{Al-PCM} is lower under HF condition that under T condition, due to more regular melting. The larger difference in the index is observed between P and D. In the P structure, ΔT_{Al-PCM} is the

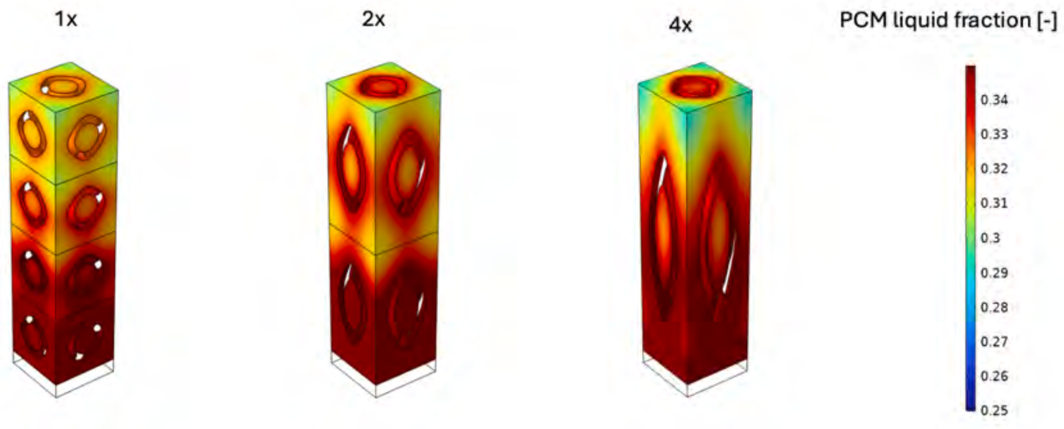

c) P Structure, HF condition

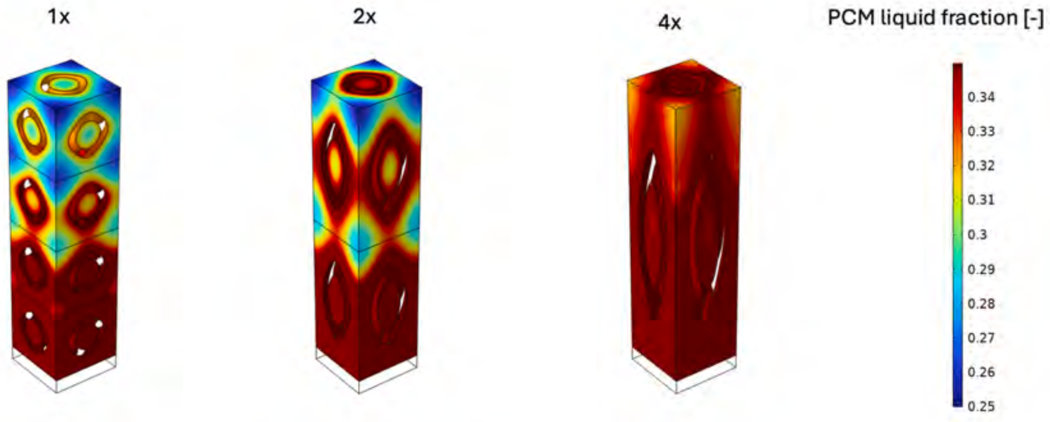

d) P Structure, T condition

Fig. 11. (*continued*).

highest and the most significantly affected by the stretching level, while in the D structures is the lowest and rather unaffected by stretching. In any case, the limited temperature differences within the C-PCM are not considered critical for the stability of the composite structure.

In general, increasing the rescaling level improves the effective thermal conductivity of the composite PCM, thus facilitating heat transfer into the material and accelerating the melting process. At the same time, the rescaling operation alters the pore geometry, causing the pores to elongate along the rescaling direction. This anisotropic deformation increases the distance between the centers of the PCM domain and the highly thermally conductive phase along the direction where the thermal gradient is enhanced. As a result, the modification of the pore geometry leads to a less uniform temperature distribution within the PCM domain, and this effect becomes more pronounced as the rescaling intensity increases.

Since temperature inhomogeneity is defined as the difference between the average temperatures of the AlSi10Mg and PCM domains, it inherently reflects the presence of local temperature variations within

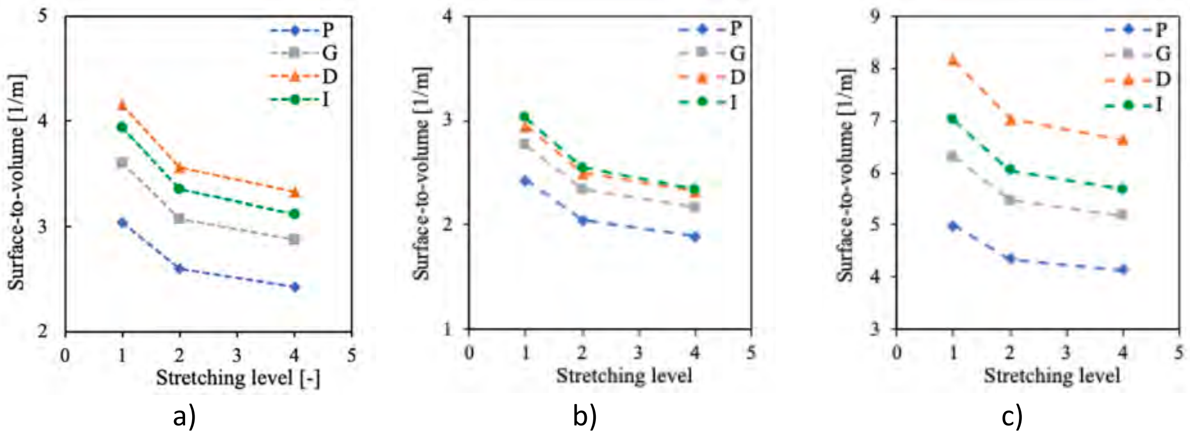

Fig. 12. Surface-to-volume ratios trends of $\varepsilon = 0.8$ TPMS structures with respect to the stretch level. (a) Referred to the whole C-PCM, whereas (b) and (c) are related to the PCM and TPMS domains only, respectively.

the PCM region. For this reason, although rescaling leads to faster thermal transients, it also increases the temperature difference between the two domains.

Regarding the comparison among the different structures, the trends observed in temperature inhomogeneity are consistent with the surface-to-volume ratio data. As shown in Fig. 12, the Diamond structure exhibits the lowest temperature inhomogeneity among the analysed configurations due to its higher surface-to-volume ratio for structures with $\varepsilon = 0.8$. This characteristic enables more efficient heat transfer across the interface between the two phases. The trends observed for the surface-to-volume ratio are further confirmed in [93,94]. This result confirms that the topology of the metallic skeleton plays a crucial role in controlling both heat transfer efficiency and temperature uniformity within the composite PCM.

4. Conclusions

This study investigates the possibility of modifying the thermophysical properties of hybrid or fully metallic composites, specifically of Al—C80 and Al—Sn intended for use as C-PCMs, by changing in one direction the geometrical scale of the metallic lattice. From the practical point of view, the geometrical rescaling can be easily obtained by Additive Manufacturing techniques.

TPMS-based composites, typically characterized by material symmetry (i.e., orthotropy or threefold cubic symmetry) may be transformed by purely geometric rescaling to achieve anisotropic thermal conductivity. The specific types of TPMS here considered to produce C-PCMs are characterized by a lattice made of the high thermal conductivity Al-based alloys, and by high levels of porosity. The porosity volume is filled either with organic PCM or Sn. Thermal conduction finite element analyses have been performed to estimate the variation on thermal conductivity along the rescaling direction and perpendicularly to it. The results are analysed in terms of original TPMS structure, rescaling level, porosity of the lattice, and thermal conductivity ratio r.

Results show that the unidimensional geometrical rescaling causes in all the structures an increment in the effective thermal conductivity along the rescaling direction and a reduction of the effective thermal conductivity in the directions perpendicular to the rescaling. This effect is highest for the Primitive-Schwarz lattice structure, lowest for the I-graph one.

It can be observed that the highest gain/reduction in the effective thermal conductivity is obtained at the rescaling level $N = 2$, independently of the composite structure, while higher rescaling reduces progressively their beneficial effects.

The presence of a metallic skeleton justifies the sensible larger increment in the effective thermal conductivity components for the Al—C80 composite relative to the Al—Sn composite, for all the levels of rescaling and porosity considered. Thus, the rescaling operations are more effective in modifying the thermal conductivity of Al—C80 composites than Al—Sn composites. In general, Al—Sn composites are less sensitive to the changes in rescaling level and porosity.

The effectiveness of rescaling operations is also tested in transient regime under different heat inputs. In general, increasing the rescaling level of the C-PCM leads to a reduction in the PCM melting time but offers a less homogeneous temperature distribution. While rescaling the C-PCM has beneficial effects on energy storage via PCM because of the increased thermal conductivity for all the investigated structures, the difficulty for heat to efficiently reach the entire domain may reduce the efficiency of the geometrical changes. In particular, the D structure exhibits the best topology for attaining the lowest temperature differences. While the beneficial effects are small in the investigated structures, where the cubic cell side is 5 mm and total height is 20 mm, they can become relevant and need to be considered for higher composite structures and larger cell sizes.

The different response of the analysed geometries to the rescaling operation is mainly related to their intrinsic morphological characteristics. Geometries with a more isotropic distribution of surfaces and a well-connected metallic skeleton tend to preserve more effective heat conduction paths even after stretching. Conversely, structures characterized by preferential orientations of the surfaces experience a stronger distortion of the pore morphology during rescaling, which increases the distance between the PCM domains and the conductive phase. As a result, the efficiency of the heat transfer pathways is affected differently depending on the geometry, explaining why some structures appear more suited to the rescaling operation than others.

The study provides a quantitative mapping of anisotropy as a function of scaling level and porosity, clarifying how microstructural rescaling affects the macroscopic thermal response. It also identifies topology-dependent behaviours under geometric stretching, showing that the evolution of thermal properties cannot be interpreted independently of structural connectivity. The outcomes of the analysis include the trade-off between melting acceleration and temperature uniformity, highlighting the competing mechanisms that govern heat transfer and phase transition.

Overall, this research clarifies the role of anisotropic geometric rescaling as a design parameter for controlling heat transport in TPMS-based composite PCMs. The numerical analyses demonstrate that unidirectional rescaling systematically modifies the effective thermal conductivity tensor, increasing the conductivity along the rescaling direction while reducing it in the transverse ones, thus promoting preferential heat transfer within the composite. The most pronounced variations occur at relatively low rescaling levels, indicating that moderate geometric stretching is sufficient to significantly alter the conductive behaviour, whereas further rescaling leads to progressively smaller improvements. In addition, the response of the composite is strongly influenced by the topology of the TPMS skeleton, as different geometries exhibit different sensitivities to the rescaling operation and different levels of temperature homogeneity during PCM melting. These results confirm that the macroscopic thermal response of TPMS-based composites derives from the combined effects of material properties, porosity, and geometric connectivity of the lattice architecture.

The results of this study suggest considering the adoption of these structures in applications where the thermal power to be transferred is high but is supplied by a source characterized by a limited heat exchange surface. In this context, the stretching operation becomes particularly beneficial, as it allows heat to be conveyed more effectively toward regions farther from the heat source.

To obtain a full characterization of C-PCMs based TPMS lattices undergoing anisotropic geometry rescaling, beyond the present results concerning thermal conductivity of structures filled by organic (C80 paraffin) and metallic (Sn) PCM, further studies should be pursued. The effect of combined rescaling and lattice size should also be considered, at least within the feasibility range for manufacturing these structures.

CRediT authorship contribution statement

Matteo Molteni: Writing – review & editing, Writing – original draft, Visualization, Software, Methodology, Investigation, Formal analysis, Data curation, Conceptualization. **Anna Pandolfi:** Writing – review & editing, Visualization, Validation, Supervision, Methodology, Conceptualization. **Elisabetta Gariboldi:** Writing – review & editing, Visualization, Validation, Supervision, Methodology, Conceptualization.

Declaration of competing interest

The authors declare that they have no known competing financial interests or personal relationships that could have appeared to influence the work reported in this paper.

Appendix A

Table A1

Al-C80 composite. Best fitting equations describing the trend of the microstructural efficiency η in x, y and z directions for porosity values ε of 0.7, 0.8 and 0.9 as a function the rescaling ratio N in z direction for (1 ≤ N ≤ 5) for each structure type. Fitting curves for porosity ε = 0.8 fits data presented in Fig. 4a (for Al-C80 phase combination),

Structure	Al-C80	Porosity ε		
		0.7	0.8	0.9
P	$\eta_{eff,x}$	$-0,0193N^2-0,1938N+0,8719$	$-0,0202N^2-0,208N+0,8682$	$-0,0202N^2-0,208N+0,8682$
	$\eta_{eff,y}$	$-0,0193N^2-0,1938N+0,8719$	$-0,0202N^2-0,208N+0,8682$	$-0,0202N^2-0,208N+0,8682$
	$\eta_{eff,z}$	$-0,0031N^4+0,0465N^3-0,2617N^2+0,6746N+0,2448$	$-0,0032N^4+0,048N^3-0,27N^2+0,6952N+0,2137$	$-0,0032N^4+0,048N^3-0,27N^2+0,6952N+0,2137$
G	$\eta_{eff,x}$	$-0,0193N^2-0,1891N+0,8234$	$-0,0201N^2-0,1954N+0,8094$	$-0,0201N^2-0,1954N+0,8094$
	$\eta_{eff,y}$	$-0,0101N^2-0,098N+0,742$	$-0,0106N^2-0,1037N+0,7295$	$-0,0106N^2-0,1037N+0,7295$
	$\eta_{eff,z}$	$-0,0024N^4+0,0372N^3-0,2163N^2+0,5938N+0,2463$	$-0,0025N^4+0,0379N^3-0,2202N^2+0,6039N+0,2202$	$-0,0025N^4+0,0379N^3-0,2202N^2+0,6039N+0,2202$
D	$\eta_{eff,x}$	$-0,0114N^2-0,1171N+0,7551$	$-0,0115N^2-0,1209N+0,7254$	$-0,0115N^2-0,1209N+0,7254$
	$\eta_{eff,y}$	$-0,0114N^2-0,1171N+0,7551$	$-0,0115N^2-0,1209N+0,7254$	$-0,0115N^2-0,1209N+0,7254$
	$\eta_{eff,z}$	$-0,0031N^4+0,0444N^3-0,245N^2+0,6383N+0,2175$	$-0,0011N^4+0,0224N^3-0,1588N^2+0,5083N+0,2491$	$-0,0011N^4+0,0224N^3-0,1588N^2+0,5083N+0,2491$
I	$\eta_{eff,x}$	$-0,0084N^2-0,1097N+0,8029$	$-0,007N^2-0,1019N+0,7507$	$-0,007N^2-0,1019N+0,7507$
	$\eta_{eff,y}$	$-0,0084N^2-0,1097N+0,8029$	$-0,007N^2-0,1019N+0,7507$	$-0,007N^2-0,1019N+0,7507$
	$\eta_{eff,z}$	$-0,0009N^4+0,0036N^3-0,0205N^2+0,1406N+0,5889$	$-0,0014N^4+0,0223N^3-0,1293N^2+0,3551N+0,4102$	$-0,0014N^4+0,0223N^3-0,1293N^2+0,3551N+0,4102$

Table A2

Al-Sn composite. Best fitting equations describing the trend of the microstructural efficiency η in x, y and z directions for porosity values ε of 0.7, 0.8 and 0.9 as a function the rescaling ratio N in z direction for (1 ≤ N ≤ 5) for each structure type. Fitting curves for porosity ε = 0.8 fits data presented in Fig. 4b (for Al-Sn phase combination).

Structure	Al-Sn	Porosity ε		
		0.7	0.8	0.9
P	$\eta_{eff,x}$	$-0,0033N^2-0,0298N+0,9597$	$-0,0027N^2-0,0233N+0,9663$	$-0,0011N^2-0,0103N+0,9755$
	$\eta_{eff,y}$	$-0,0033N^2-0,0298N+0,9597$	$-0,0027N^2-0,0233N+0,9663$	$-0,0011N^2-0,0103N+0,9755$
	$\eta_{eff,z}$	$-0,0006N^4+0,0095N^3-0,0539N^2+0,1418N+0,8386$	$-0,0005N^4+0,076N^3-0,0433N^2+0,1147N+0,8682$	$-0,0003N^4+0,0046N^3-0,0246N^2+0,0701N+0,9198$
G	$\eta_{eff,x}$	$-0,0018N^2-0,0177N+0,9468$	$-0,0016N^2-0,0151N+0,9543$	$-0,0014N^2-0,012N+0,9746$
	$\eta_{eff,y}$	$-0,0025N^2-0,0221N+0,9506$	$-0,002N^2-0,0182N+0,9586$	$-0,0013N^2-0,0111N+0,9739$
	$\eta_{eff,z}$	$-0,0005N^4+0,0074N^3-0,0434N^2+0,1211N+0,8475$	$-0,0004N^4+0,0059N^3-0,035N^2+0,0975N+0,8752$	$-0,0002N^4+0,0037N^3-0,0216N^2+0,0598N+0,9229$
D	$\eta_{eff,x}$	$-0,0026N^2-0,0225N+0,9499$	$-0,0021N^2-0,0183N+0,9573$	$-0,0012N^2-0,0109N+0,9696$
	$\eta_{eff,y}$	$-0,0026N^2-0,0225N+0,9499$	$-0,0021N^2-0,0183N+0,9573$	$-0,0012N^2-0,0109N+0,9696$
	$\eta_{eff,z}$	$-0,0007N^4+0,0101N^3-0,0556N^2+0,1419N+0,835$	$-0,0002N^4+0,0011N^3-0,0082N^2+0,0575N+0,8934$	$-0,0003N^4+0,0045N^3-0,0263N^2+0,0674N+0,9147$
I	$\eta_{eff,x}$	$-0,0018N^2-0,0177N+0,9468$	$-0,0016N^2-0,0151N+0,9543$	$-0,0015N^2-0,0121N+0,973$
	$\eta_{eff,y}$	$-0,0018N^2-0,0177N+0,9468$	$-0,0016N^2-0,0151N+0,9543$	$-0,0015N^2-0,0121N+0,973$
	$\eta_{eff,z}$	$-0,0003N^4+0,0043N^3-0,0252N^2+0,0738N+0,8789$	$-0,00005N^4+0,002N^3-0,017N^2+0,0569N+0,8998$	$0,0008N^3-0,082N^2+0,0312N+0,9386$

Table A3

Al-C80 composite. Best fitting equations describing the trend of the morphological efficiency μ in x, y and z directions for porosity values ε of 0.7, 0.8 and 0.9 as a function the rescaling ratio N in z direction for (1 ≤ N ≤ 5) for each structure type. Fitting curves for porosity ε = 0.8 fits data presented in Fig. 6a (for Al-C80 phase combination).

Structure	Al-C80	Porosity ε		
		0.7	0.8	0.9
P	$\mu_{eff,x}$	$0,0195N^2-0,1961N+0,8704$	$0,0205N^2-0,2112N+0,8662$	$0,021N^2-0,222N+0,87$
	$\mu_{eff,y}$	$0,0195N^2-0,1961N+0,8704$	$0,0205N^2-0,2112N+0,8662$	$0,021N^2-0,222N+0,87$
	$\mu_{eff,z}$	$-0,0031N^4+0,047N^3-0,2648N^2+0,6824N+0,236$	$-0,0033N^4+0,0487N^3-0,2741N^2+0,7058N+0,2017$	$-0,0033N^4+0,05N^3-0,2809N^2+0,721N+0,1852$
G	$\mu_{eff,x}$	$0,0196N^2-0,1913N+0,8214$	$0,0204N^2-0,1984N+0,8065$	$0,0195N^2-0,1924N+0,7765$

(continued on next page)

Table A3 (*continued*)

Structure	Al-C80	Porosity ε		
		0.7	0.8	0.9
	$\mu_{eff,y}$	$0,0102N^2 - 0,0991N + 0,739$	$0,0205N^2 - 0,211N + 0,8662$	$0,0107N^2 - 0,1076N + 0,7118$
	$\mu_{eff,z}$	$-0,0025N^4 + 0,0376N^3 - 0,2188N^2 + 0,6007N + 0,2375$	$-0,0025N^4 + 0,0385N^3 - 0,2236N^2 + 0,6131N + 0,2083$	$-0,0026N^4 + 0,0399N^3 - 0,2303N^2 + 0,626N + 0,1846$
D	$\mu_{eff,x}$	$0,0115N^2 - 0,1185N + 0,7523$	$0,0117N^2 - 0,1227N + 0,7212$	$0,0118N^2 - 0,1238N + 0,6712$
	$\mu_{eff,y}$	$0,0115N^2 - 0,1185N + 0,7523$	$0,0117N^2 - 0,1227N + 0,7212$	$0,0118N^2 - 0,1238N + 0,6712$
	$\mu_{eff,z}$	$-0,0031N^4 + 0,0449N^3 - 0,2479N^2 + 0,6457N + 0,2084$	$-0,0012N^4 + 0,0227N^3 - 0,1612N^2 + 0,516N + 0,2376$	$-0,0031N^4 + 0,0449N^3 - 0,2474N^2 + 0,6431N + 0,1255$
I	$\mu_{eff,x}$	$0,0085N^2 - 0,111N + 0,8006$	$0,0072N^2 - 0,1035N + 0,7469$	$0,0079N^2 - 0,1125N + 0,7369$
	$\mu_{eff,y}$	$0,0085N^2 - 0,111N + 0,8006$	$0,0072N^2 - 0,1035N + 0,7469$	$0,0079N^2 - 0,1125N + 0,7369$
	$\mu_{eff,z}$	$-0,0009N^4 + 0,0037N^3 - 0,0207N^2 + 0,1422N + 0,5841$	$-0,0015N^4 + 0,0226N^3 - 0,1313N^2 + 0,3605N + 0,4012$	$0,0079N^3 - 0,0802N^2 + 0,2875N + 0,4165$

Table A4

Al-Sn composite. Best fitting equations describing the trend of the morphological efficiency μ in x, y and z directions for porosity values ε of 0.7, 0.8 and 0.9 as a function the rescaling ratio N in z direction for ($1 \le N \le 5$) for each structure type. Fitting curves for porosity $\varepsilon = 0.8$ fits data presented in Fig. 6b (for Al-C80 phase combination).

Structure	Al-Sn	Porosity ε		
		0.7	0.8	0.9
P	$\mu_{eff,x}$	$-0,0159N^2 + 0,1398N + 0,805$	$-0,0161N^2 + 0,1409N + 0,7967$	$0,011N^2 - 0,1023N + 0,756$
	$\mu_{eff,y}$	$-0,0159N^2 + 0,1398N + 0,805$	$-0,0161N^2 + 0,1409N + 0,7967$	$0,011N^2 - 0,1023N + 0,756$
	$\mu_{eff,z}$	$-0,003N^4 + 0,0458N^3 - 0,2609N^2 + 0,6861N + 0,2191$	$-0,003N^4 + 0,0457N^3 - 0,2615N^2 + 0,6924N + 0,2043$	$-0,0003N^4 + 0,0458N^3 - 0,2625N^2 + 0,6982N + 0,2016$
G	$\mu_{eff,x}$	$0,0144N^2 - 0,128N + 0,7794$	$0,0142N^2 - 0,1256N + 0,7638$	$0,0135N^2 - 0,1193N + 0,7474$
	$\mu_{eff,y}$	$0,0121N^2 - 0,1067N + 0,761$	$0,0124N^2 - 0,1097N + 0,7502$	$0,0125N^2 - 0,1109N + 0,7405$
	$\mu_{eff,z}$	$-0,0023N^4 + 0,0357N^3 - 0,2102N^2 + 0,586N + 0,2619$	$-0,0023N^4 + 0,0358N^3 - 0,2111N^2 + 0,589N + 0,2462$	$-0,0024N^4 + 0,0367N^3 - 0,2148N^2 + 0,5953N + 0,2319$
D	$\mu_{eff,x}$	$-0,0125N^2 + 0,1088N + 0,7575$	$-0,0126N^2 + 0,1102N + 0,7422$	$0,0123N^2 - 0,1081N + 0,6978$
	$\mu_{eff,y}$	$-0,0125N^2 + 0,1088N + 0,7575$	$-0,0126N^2 + 0,1102N + 0,7422$	$0,0123N^2 - 0,1081N + 0,6978$
	$\mu_{eff,z}$	$-0,0033N^4 + 0,0487N^3 - 0,2689N^2 + 0,6868N + 0,2014$	$-0,0014N^4 + 0,0068N^3 - 0,2689N^2 + 0,6868N + 0,2014$	$-0,0026N^4 + 0,0444N^3 - 0,2621N^2 + 0,6709N + 0,1506$
I	$\mu_{eff,x}$	$-0,0087N^2 + 0,0855N + 0,7424$	$0,0094N^2 + 0,0909N + 0,7242$	$0,0153N^2 + 0,1203N + 0,7309$
	$\mu_{eff,y}$	$-0,0087N^2 + 0,0855N + 0,7424$	$0,0094N^2 + 0,0909N + 0,7242$	$0,0153N^2 + 0,1203N + 0,7309$
	$\mu_{eff,z}$	$-0,0013N^4 + 0,0206N^3 - 0,1221N^2 + 0,3571N + 0,4139$	$-0,0003N^4 + 0,0122N^3 - 0,1029N^2 + 0,3438N + 0,395$	$-0,0079N^3 + 0,0817N^2 - 0,3104N + 0,3885$

Table A5

Al-C80 composite. Best fitting equations describing the trend of the microstructural efficiency η in x, y and z directions for rescaling ratio N in z direction of 1, 2, 3, 4, 5 as a function the porosity ($0.7 \le \varepsilon \le 0.9$) for each structure type. For $\varepsilon = 0.8$, equations cover data presented in Fig. 7a.

Structure	Al-C80	Geometric rescaling level N				
		1	2	3	4	5
P	$\eta_{eff,x}$	$-0,1016\varepsilon + 0,7698$	$-0,1851\varepsilon + 0,6806$	$-0,2793\varepsilon + 0,656$	$-0,3521\varepsilon + 0,655$	$-0,4066\varepsilon + 0,6619$
	$\eta_{eff,y}$	$-0,1016\varepsilon + 0,7698$	$-0,1851\varepsilon + 0,6806$	$-0,2794\varepsilon + 0,656$	$-0,3521\varepsilon + 0,655$	$-0,4063\varepsilon + 0,6616$
	$\eta_{eff,z}$	$-0,1016\varepsilon + 0,7698$	$-0,0734\varepsilon + 0,9188$	$-0,0668\varepsilon + 0,9616$	$-0,062\varepsilon + 0,9774$	$-0,0579\varepsilon + 0,9841$
G	$\eta_{eff,x}$	$-0,1543\varepsilon + 0,7653$	$-0,1854\varepsilon + 0,6401$	$-0,1979\varepsilon + 0,5676$	$-0,2001\varepsilon + 0,5226$	$-0,2015\varepsilon + 0,4952$
	$\eta_{eff,y}$	$-0,1543\varepsilon + 0,7653$	$-0,1738\varepsilon + 0,7005$	$-0,1996\varepsilon + 0,6778$	$-0,2221\varepsilon + 0,6703$	$-0,2407\varepsilon + 0,6689$
	$\eta_{eff,z}$	$-0,1543\varepsilon + 0,7653$	$-0,146\varepsilon + 0,9288$	$-0,1468\varepsilon + 0,9915$	$-0,1488\varepsilon + 1,0211$	$-0,1478\varepsilon + 1,0371$
D	$\eta_{eff,x}$	$-0,3873\varepsilon + 0,9254$	$-0,4101\varepsilon + 0,8464$	$-0,4244\varepsilon + 0,8061$	$-0,4444\varepsilon + 0,7873$	$-0,4575\varepsilon + 0,7716$
	$\eta_{eff,y}$	$-0,3873\varepsilon + 0,9254$	$-0,4045\varepsilon + 0,8423$	$-0,422\varepsilon + 0,8042$	$-0,4434\varepsilon + 0,7866$	$-0,4594\varepsilon + 0,7731$
	$\eta_{eff,z}$	$-0,3873\varepsilon + 0,9254$	$-0,4026\varepsilon + 1,1058$	$-0,3958\varepsilon + 1,1611$	$-0,3617\varepsilon + 1,1643$	$-0,2854\varepsilon + 1,1233$
I	$\eta_{eff,x}$	$-0,3239\varepsilon + 0,9273$	$-0,263\varepsilon + 0,7888$	$-0,331\varepsilon + 0,7797$	$-0,3943\varepsilon + 0,7793$	$-0,4428\varepsilon + 0,7709$
	$\eta_{eff,y}$	$-0,3239\varepsilon + 0,9273$	$-0,2539\varepsilon + 0,7809$	$-0,3444\varepsilon + 0,7911$	$-0,2762\varepsilon + 0,6768$	$-0,2312\varepsilon + 0,6014$
	$\eta_{eff,z}$	$-0,3239\varepsilon + 0,9273$	$-0,1597\varepsilon + 0,8853$	$-0,1097\varepsilon + 0,8787$	$-0,0964\varepsilon + 0,8867$	$-0,4196\varepsilon + 1,1658$

Table A6
Al-Sn composite. Best fitting equations describing the trend of the microstructural efficiency η in x, y and z directions for rescaling ratio N in z direction of 1, 2, 3, 4, 5 as a function the porosity ($0.7\leq \varepsilon \leq 0.9$) for each structure type. For $\varepsilon = 0.8$, equations cover data presented in Fig. 7b.

Structure	Al-Sn	Geometric rescaling level N				
		1	2	3	4	5
P	$\eta_{eff,x}$	$-0,1628\varepsilon+0,8197$	$-0,2223\varepsilon+0,7547$	$-0,2476\varepsilon+0,7273$	$-0,2971\varepsilon+0,691$	$-0,2653\varepsilon+0,7082$
	$\eta_{eff,y}$	$-0,1628\varepsilon+0,8197$	$-0,2223\varepsilon+0,7547$	$-0,2476\varepsilon+0,7273$	$-0,2912\varepsilon+0,6914$	$-0,2654\varepsilon+0,7081$
	$\eta_{eff,z}$	$-0,1628\varepsilon+0,8197$	$-0,072\varepsilon+0,9209$	$-0,0461\varepsilon+0,9505$	$-0,036\varepsilon+0,9624$	$-0,0314\varepsilon+0,968$
G	$\eta_{eff,x}$	$-0,1625\varepsilon+0,8166$	$-0,2197\varepsilon+0,7552$	$-0,24476\varepsilon+0,7288$	$-0,2573\varepsilon+0,7154$	$-0,264\varepsilon+0,7082$
	$\eta_{eff,y}$	$-0,1625\varepsilon+0,8166$	$-0,2063\varepsilon+0,7696$	$-0,2234\varepsilon+0,7486$	$-0,2318\varepsilon+0,7392$	$-0,2363\varepsilon+0,7341$
	$\eta_{eff,z}$	$-0,1625\varepsilon+0,8166$	$-0,0727\varepsilon+0,9154$	$-0,0397\varepsilon+0,9517$	$-0,0245\varepsilon+0,9687$	$-0,0163\varepsilon+0,9779$
D	$\eta_{eff,x}$	$-0,1463\varepsilon+0,8271$	$-0,1943\varepsilon+0,7752$	$-0,2122\varepsilon+0,7556$	$-0,2199\varepsilon+0,7413$	$-0,2251\varepsilon+0,7413$
	$\eta_{eff,y}$	$-0,1463\varepsilon+0,8271$	$-0,1943\varepsilon+0,7752$	$-0,2114\varepsilon+0,7563$	$-0,221\varepsilon+0,746$	$-0,2253\varepsilon+0,7412$
	$\eta_{eff,z}$	$-0,1463\varepsilon+0,8271$	$-0,0482\varepsilon+0,932$	$-0,0136\varepsilon+0,9678$	$-0,0027\varepsilon+0,9787$	$-0,0275\varepsilon+0,9621$
I	$\eta_{eff,x}$	$-0,1546\varepsilon+0,8214$	$-0,1883\varepsilon+0,7835$	$-0,2006\varepsilon+0,7676$	$-0,2171\varepsilon+0,751$	$-0,1477\varepsilon+0,7996$
	$\eta_{eff,y}$	$-0,1546\varepsilon+0,8214$	$-0,1883\varepsilon+0,7834$	$-0,2064\varepsilon+0,7633$	$-0,2172\varepsilon+0,751$	$-0,1478\varepsilon+0,7995$
	$\eta_{eff,z}$	$-0,1546\varepsilon+0,8214$	$-0,0962\varepsilon+0,8866$	$-0,0692\varepsilon+0,9158$	$-0,0531\varepsilon+0,9332$	$-0,0541\varepsilon+0,9382$

Table A7
Al-C80 composite. Best fitting equations describing the trend of the morphological efficiency μ in x, y and z directions for rescaling ratio N in z direction of 1, 2, 3, 4, 5 as a function the porosity ($0.7\leq \varepsilon \leq 0.9$) for each structure type. For $\varepsilon = 0.8$, equations cover data presented in Fig. 8a.

Structure	Al-C80	Geometric rescaling level N				
		1	2	3	4	5
P	$\mu_{eff,x}$	$-0,1275\varepsilon+0,7848$	$-0,2246\varepsilon+0,7037$	$-0,3284\varepsilon+0,6848$	$-0,4071\varepsilon+0,6875$	$-0,4656\varepsilon+0,6969$
	$\mu_{eff,y}$	$-0,1275\varepsilon+0,7848$	$-0,2246\varepsilon+0,7037$	$-0,3284\varepsilon+0,6848$	$-0,4071\varepsilon+0,6875$	$-0,4656\varepsilon+0,6969$
	$\mu_{eff,z}$	$-0,1275\varepsilon+0,7848$	$-0,0855\varepsilon+0,9259$	$-0,0751\varepsilon+0,9666$	$-0,0686\varepsilon+0,9815$	$-0,0638\varepsilon+0,9876$
G	$\mu_{eff,x}$	$-0,2332\varepsilon+0,8187$	$-0,2282\varepsilon+0,6651$	$-0,2472\varepsilon+0,5964$	$-0,2532\varepsilon+0,5535$	$-0,2568\varepsilon+0,5273$
	$\mu_{eff,y}$	$-0,1208\varepsilon+0,7552$	$-0,1367\varepsilon+0,6808$	$-0,1474\varepsilon+0,6539$	$-0,1531\varepsilon+0,641$	$-0,1578\varepsilon+0,6349$
	$\mu_{eff,z}$	$-0,1849\varepsilon+0,7832$	$-0,1643\varepsilon+0,9392$	$-0,1614\varepsilon+0,9993$	$-0,1593\varepsilon+1,0276$	$-0,1569\varepsilon+1,0429$
D	$\mu_{eff,x}$	$-0,4307\varepsilon+0,9536$	$-0,4554\varepsilon+0,8737$	$-0,474\varepsilon+0,8359$	$-0,497\varepsilon+0,8189$	$-0,5124\varepsilon+0,8046$
	$\mu_{eff,y}$	$-0,4307\varepsilon+0,9536$	$-0,4554\varepsilon+0,8737$	$-0,474\varepsilon+0,8359$	$-0,497\varepsilon+0,8189$	$-0,5124\varepsilon+0,8046$
	$\mu_{eff,z}$	$-0,4247\varepsilon+0,9482$	$-0,4275\varepsilon+1,1216$	$-0,4159\varepsilon+1,1742$	$-0,3786\varepsilon+1,1754$	$-0,2992\varepsilon+1,1324$
I	$\mu_{eff,x}$	$-0,3581\varepsilon+0,9437$	$-0,3005\varepsilon+0,8111$	$-0,3747\varepsilon+0,8057$	$-0,4332\varepsilon+0,8086$	
	$\mu_{eff,y}$	$-0,3581\varepsilon+0,9437$	$-0,3005\varepsilon+0,8111$	$-0,3747\varepsilon+0,8057$	$-0,4332\varepsilon+0,8086$	
	$\mu_{eff,z}$	$-0,3554\varepsilon+0,9464$	$-0,1816\varepsilon+0,8984$	$-0,1282\varepsilon+0,8897$	$-0,1132\varepsilon+0,8967$	

Table A8
Al-Sn composite. Best fitting equations describing the trend of the morphological efficiency μ in x, y and z directions for rescaling ratio N in z direction of 1, 2, 3, 4, 5 as a function the porosity ($0.7\leq \varepsilon \leq 0.9$) for each structure type. For $\varepsilon = 0.8$, equations cover data presented in Fig. 8b.

Structure	Al-Sn	Geometric rescaling level N				
		1	2	3	4	5
P	$\mu_{eff,x}$	$-0,0346\varepsilon+0,7094$	$-0,027\varepsilon+0,5928$	$-0,0149\varepsilon+0,5386$	$0,315\varepsilon+0,2758$	$-0,0094\varepsilon+0,5022$
	$\mu_{eff,y}$	$-0,0346\varepsilon+0,7094$	$-0,027\varepsilon+0,5928$	$-0,0149\varepsilon+0,5386$	$0,315\varepsilon+0,2758$	$-0,0094\varepsilon+0,5022$
	$\mu_{eff,z}$	$-0,0346\varepsilon+0,7094$	$0,0047\varepsilon+0,8602$	$0,0328\varepsilon+0,8946$	$0,00523\varepsilon+0,9036$	$0,0661\varepsilon+0,9051$
G	$\mu_{eff,x}$	$-0,1208\varepsilon+0,7552$	$-0,0894\varepsilon+0,6313$	$-0,0677\varepsilon+0,5731$	$-0,054\varepsilon+0,5421$	$-0,0486\varepsilon+0,5267$
	$\mu_{eff,y}$	$-0,1758\varepsilon+0,7755$	$-0,211\varepsilon+0,7222$	$-0,2406\varepsilon+0,7018$	$-0,1531\varepsilon+0,641$	$-0,1578\varepsilon+0,6349$
	$\mu_{eff,z}$	$-0,0346\varepsilon+0,7094$	$-0,1143\varepsilon+0,9213$	$-0,1114\varepsilon+0,982$	$-0,1062\varepsilon+1,0081$	$-0,1011\varepsilon+1,0211$
D	$\mu_{eff,x}$	$-0,2953\varepsilon+0,8774$	$-0,296\varepsilon+0,7897$	$-0,2912\varepsilon+0,753$	$-0,2961\varepsilon+0,7405$	$-0,2958\varepsilon+0,7311$
	$\mu_{eff,y}$	$-0,2953\varepsilon+0,8774$	$-0,296\varepsilon+0,7897$	$-0,2912\varepsilon+0,753$	$-0,2961\varepsilon+0,7405$	$-0,2958\varepsilon+0,7311$
	$\mu_{eff,z}$	$-0,3171\varepsilon+0,8917$	$-0,3892\varepsilon+1,1157$	$-0,466\varepsilon+1,2264$	$-0,4549\varepsilon+1,2323$	$-0,1745\varepsilon+1,0348$
I	$\mu_{eff,x}$	$-0,2153\varepsilon+0,8193$	$-0,2362\varepsilon+0,7656$	$-0,3018\varepsilon+0,7781$	$-0,249\varepsilon+0,7155$	$-0,2708\varepsilon+0,7205$
	$\mu_{eff,y}$	$-0,2153\varepsilon+0,8193$	$-0,2362\varepsilon+0,7656$	$-0,3018\varepsilon+0,7781$	$-0,249\varepsilon+0,7155$	$-0,2708\varepsilon+0,7205$
	$\mu_{eff,z}$	$-0,2153\varepsilon+0,8193$	$-0,1886\varepsilon+0,9152$	$-0,1868\varepsilon+0,9623$	$-0,1883\varepsilon+0,9919$	$0,0398\varepsilon+0,8565$

Table A9
Comparison among effective thermal conductivities of upstretched structures obtained in [30] and the present work.

Thermal conductivity [W/(m*K)]				
Structure	G	P	I	K
Reference paper [30]	10.54	11.7	11.16	7.06
This work	10.74	11.78	11.27	7.22

Table A10
Comparison among effective thermal conductivities of stretched structures obtained in [63] and the present work.

Thermal conductivity [W/(m*K)]		
Structure	P	P (2x)
Reference paper [63]	15.3	19
This work	15.24	18,972

Table A11
Comparison between the total PCM melting time in transient regime simulations obtained in [30] and the present work.

PCM melting time [s]	
Reference paper [30]	This work
267.8	258.3

Data availability

The authors do not have permission to share data.

References

[1] O. Al-Ketan, D.W. Lee, R. Rowshan, R.K. Abu Al-Rub, Functionally graded and multi-morphology sheet TPMS lattices: design, manufacturing, and mechanical properties, J. Mech. Behav. Biomed. Mater. 102 (November 2019) (2020) 103520, https://doi.org/10.1016/j.jmbbm.2019.103520.

[2] O. Al-Ketan, A. Soliman, A.M. AlQubaisi, R.K. Abu Al-Rub, Nature-inspired lightweight cellular co-continuous composites with architected periodic gyroidal structures, Adv. Eng. Mater. 20 (2) (2018) 1–9, https://doi.org/10.1002/adem.201700549.

[3] J. Pérez, A new golden age of minimal surfaces, Not. Am. Math. Soc. 64 (04) (2017) 347–358, https://doi.org/10.1090/noti1500.

[4] O. Al-Ketan, R.K. Abu Al-Rub, Multifunctional mechanical metamaterials based on triply periodic minimal surface lattices, Adv. Eng. Mater. 21 (10) (2019) 1–39, https://doi.org/10.1002/adem.201900524.

[5] J. Feng, J. Fu, X. Yao, Y. He, Triply periodic minimal surface (TPMS) porous structures: from multi-scale design, precise additive manufacturing to multidisciplinary applications, Int. J. Extreme Manuf. 4 (2) (2022), https://doi.org/10.1088/2631-7990/ac5be6.

[6] S. Yu, J. Sun, J. Bai, Investigation of functionally graded TPMS structures fabricated by additive manufacturing, Mater. Des. 182 (2019) 108021, https://doi.org/10.1016/j.matdes.2019.108021.

[7] M. Jin, et al., Investigation on the mechanical properties of TPMS porous structures fabricated by laser powder bed fusion, J. Manuf. Process. 76 (November 2021) (2022) 559–574, https://doi.org/10.1016/j.jmapro.2022.02.035.

[8] B.W. Reynolds, C.J. Fee, K.R. Morison, D.J. Holland, Characterisation of heat transfer within 3D printed TPMS heat exchangers, Int. J. Heat Mass Transf. 212 (2023), https://doi.org/10.1016/j.ijheatmasstransfer.2023.124264.

[9] J. Santos, T. Pires, B.P. Gouveia, A.P.G. Castro, P.R. Fernandes, On the permeability of TPMS scaffolds, J. Mech. Behav. Biomed. Mater. 110 (June) (2020) 1–7, https://doi.org/10.1016/j.jmbbm.2020.103932.

[10] B.B. Ravichander, S.H. Jagdale, A. Jabed, G. Kumar, Mechanical and corrosion behavior of sheet-based 316L TPMS structures, Int. J. Mech. Sci. 254 (May) (2023) 108439, https://doi.org/10.1016/j.ijmecsci.2023.108439.

[11] N. Qiu, Y. Wan, Y. Shen, J. Fang, Experimental and numerical studies on mechanical properties of TPMS structures, Int. J. Mech. Sci. 261 (March 2023) (2024) 108657, https://doi.org/10.1016/j.ijmecsci.2023.108657.

[12] S. Catchpole-Smith, R.R.J. Sélo, A.W. Davis, I.A. Ashcroft, C.J. Tuck, A. Clare, Thermal conductivity of TPMS lattice structures manufactured via laser powder bed fusion, Addit. Manuf. 30 (August) (2019) 100846, https://doi.org/10.1016/j.addma.2019.100846.

[13] N. Novak, et al., Development of novel hybrid TPMS cellular lattices and their mechanical characterisation, J. Mater. Res. Technol. 15 (2021) 1318–1329, https://doi.org/10.1016/j.jmrt.2021.08.092.

[14] J. Lu, P. Dong, Y. Zhao, Y. Zhao, Y. Zeng, 3D printing of TPMS structural ZnO ceramics with good mechanical properties, Ceram. Int. 47 (9) (2021) 12897–12905, https://doi.org/10.1016/j.ceramint.2021.01.152.

[15] S. Restrepo, S. Ocampo, J.A. Ramirez, C. Paucar, C. Garcia, Mechanical properties of ceramic structures based on triply periodic minimal surface (TPMS) processed by 3D printing, J. Phys. Conf. Ser. 935 (1) (2017) 8–14, https://doi.org/10.1088/1742-6596/935/1/012036.

[16] S. Khaleghi, F.N. Dehnavi, M. Baghani, M. Safdari, K. Wang, M. Baniassadi, On the directional elastic modulus of the TPMS structures and a novel hybridization method to control anisotropy, Mater. Des. 210 (2021) 110074, https://doi.org/10.1016/j.matdes.2021.110074.

[17] R. Attarzadeh, S.H. Attarzadeh-Niaki, C. Duwig, Multi-objective optimization of TPMS-based heat exchangers for low-temperature waste heat recovery, Appl. Therm. Eng. 212 (April) (2022) 118448, https://doi.org/10.1016/j.applthermaleng.2022.118448.

[18] M. Alteneiji, M.I.H. Ali, K.A. Khan, R.K.A. Al-Rub, Heat transfer effectiveness characteristics maps for additively manufactured TPMS compact heat exchangers, Energy Storage Saving 1 (3) (2022) 153–161, https://doi.org/10.1016/j.enss.2022.04.005.

[19] C. Lin, G. Wen, H. Yin, Z.P. Wang, J. Liu, Y.M. Xie, Revealing the sound insulation capacities of TPMS sandwich panels, J. Sound Vib. 540 (May) (2022) 117303, https://doi.org/10.1016/j.jsv.2022.117303.

[20] N.V. Viet, N. Karathanasopoulos, W. Zaki, Mechanical attributes and wave propagation characteristics of TPMS lattice structures, Mech. Mater. 172 (May) (2022) 104363, https://doi.org/10.1016/j.mechmat.2022.104363.

[21] J. Zhang, S. Xie, T. Li, Z. Liu, S. Zheng, H. Zhou, A study of multi-stage energy absorption characteristics of hybrid sheet TPMS lattices, Thin-Walled Struct. 190 (April) (2023) 110989, https://doi.org/10.1016/j.tws.2023.110989.

[22] J.W. Lee, S.H. Oh, E. Jeon, J. Kim, K. Park, Functional gradation of the morphological properties of TPMS channel for enhanced flow performance, Mater. Des. 224 (2022) 111413, https://doi.org/10.1016/j.matdes.2022.111413.

[23] S. ma, et al., Manufacturability, mechanical properties, mass-transport properties and biocompatibility of triply periodic minimal surface (TPMS) porous scaffolds fabricated by selective laser melting, Mater. Des. 195 (2020), https://doi.org/10.1016/j.matdes.2020.109034.

[24] Z. Dong, X. Zhao, Application of TPMS structure in bone regeneration, Eng. Regen. 2 (September) (2021) 154–162, https://doi.org/10.1016/j.engreg.2021.09.004.

[25] S. Wang, et al., Efficient representation and optimization of TPMS-based porous structures for 3D heat dissipation, Comput. Aided Des. 142 (2022) 103123, https://doi.org/10.1016/j.cad.2021.103123.

[26] J. Wang, K. Chen, M. Zeng, T. Ma, Q. Wang, Z. Cheng, Investigation on flow and heat transfer in various channels based on triply periodic minimal surfaces (TPMS), Energy Convers. Manag. 283 (2023) 116955, https://doi.org/10.1016/j.enconman.2023.116955.

[27] S.H. Oh, C.H. An, B. Seo, J. Kim, C.Y. Park, K. Park, Functional morphology change of TPMS structures for design and additive manufacturing of compact heat exchangers, Addit. Manuf. 76 (March) (2023) 103778, https://doi.org/10.1016/j.addma.2023.103778.

[28] K. Yeranee, Y. Rao, A review of recent investigations on flow and heat transfer enhancement in cooling channels embedded with triply periodic minimal surfaces (TPMS), Energies 15 (23) (2022), https://doi.org/10.3390/en15238994.

[29] W. Karol, T. S., A review of models for effective thermal conductivity of composite materials, J. Power Technol. 95 (1) (2011) 14–24. Available: http://papers.itc.pw.edu.pl/index.php/JPT/article/view/463 (Online).

[30] Z.A. Qureshi, S.A.B. Al-Omari, E. Elnajjar, O. Al-Ketan, R.A. Al-Rub, Using triply periodic minimal surfaces (TPMS)-based metal foams structures as skeleton for metal-foam-PCM composites for thermal energy storage and energy management applications, Int. Commun. Heat Mass Transf. 124 (April) (2021) 105265, https://doi.org/10.1016/j.icheatmasstransfer.2021.105265.

[31] M. Molteni, S. Candidori, S. Graziosi, E. Gariboldi, Improving the thermal response flexibility of 2- and 3-phase composite phase change materials by metallic triply periodic minimal surface structures, J. Energy Storage 72 (PC) (2023) 108185, https://doi.org/10.1016/j.est.2023.108185.

[32] S. Samson, P. Tran, P. Marzocca, Design and modelling of porous gyroid heatsinks: influences of cell size, porosity and material variation, Appl. Therm. Eng. 235 (2023), https://doi.org/10.1016/j.applthermaleng.2023.121296.

[33] K. Pielichowska, K. Pielichowski, Phase change materials for thermal energy storage, Prog. Mater. Sci. 65 (2014) 67–123, https://doi.org/10.1016/j.pmatsci.2014.03.005.

[34] P.J. Shamberger, N.M. Bruno, Review of metallic phase change materials for high heat flux transient thermal management applications, Appl. Energy 258 (November 2019) (2020) 113955, https://doi.org/10.1016/j.apenergy.2019.113955.

[35] A. Rawson, C. Villada, M. Kolbe, V. Stahl, F. Kargl, Suitability of aluminium copper silicon eutectic as a phase change material for thermal storage applications: Thermophysical properties and compatibility, Energy Storage September (2021) 1–15, https://doi.org/10.1002/est2.299.

[36] Z. He, H. Ma, S. Lu, Design and experimental investigation of topology-optimized fin structures for enhanced heat transfer in latent heat thermal energy storage units, J. Energy Storage 80 (January) (2024) 110272, https://doi.org/10.1016/j.est.2023.110272.

[37] S. Piacquadio, M. Schirp-Schoenen, M. Mameli, S. Filippeschi, K.U. Schröder, Experimental analysis of the thermal energy storage potential of a phase change material embedded in additively manufactured lattice structures, Appl. Therm. Eng. 216 (June) (2022), https://doi.org/10.1016/j.applthermaleng.2022.119091.

[38] B. Peng, Z. He, H. Wang, F. Su, Optimization of patterned-fins for enhancing charging performances of phase change materials-based thermal energy storage systems, Int. J. Heat Mass Transf. 164 (2021) 120573, https://doi.org/10.1016/j.ijheatmasstransfer.2020.120573.

[39] H. Sugo, E. Kisi, D. Cuskelly, Miscibility gap alloys with inverse microstructures and high thermal conductivity for high energy density thermal storage applications, Appl. Therm. Eng. 51 (1–2) (2013) 1345–1350, https://doi.org/10.1016/j.applthermaleng.2012.11.029.

[40] Z. Li, E. Gariboldi, Reliable estimation of effective thermal properties of a 2-phase material by its optimized modelling in view of Lattice Monte-Carlo simulation, Comput. Mater. Sci. 169 (June) (2019) 109125, https://doi.org/10.1016/j.commatsci.2019.109125.

[41] S. Principles, Phase-change Heat Transfer Vol. 1, 1983.

[42] H. Li, W. Zheng, W. Liu, Q. Zhu, Intrinsically and extrinsically anisotropic heat transport in bulk materials and nanostructures: a review, Int. J. Heat Mass Transf. 196 (2022) 123307, https://doi.org/10.1016/j.ijheatmasstransfer.2022.123307.

[43] X. Sun, R. Chen, N. Yang, S. Hu, Anisotropic lattice thermal conductivity in Sn2S3: role of rattling modes in phonon transport, Phys. Rev. B 112 (12) (2025) 125401, https://doi.org/10.1103/j7pb-17wn.

[44] G.A. Slack, Anisotropic thermal conductivity of pyrolytic graphite, Phys. Rev. 127 (3) (1962) 694–701, https://doi.org/10.1103/PhysRev.127.694.

[45] G. Romano, A.M. Kolpak, Thermal anisotropy enhanced by phonon size effects in nanoporous materials, Appl. Phys. Lett. 110 (9) (2017) 1–4, https://doi.org/10.1063/1.4976540.

[46] W. Aboelsoud, L. Zhou, W. Wu, L.C. Chow, Study of thermal transport in highly anisotropic materials for space recuperator applications, Case Stud. Therm. Eng. 28 (December 2020) (2021), https://doi.org/10.1016/j.csite.2021.101441.

[47] Y. Li, H. Yan, M. massoudi, W.T. Wu, Effects of anisotropic thermal conductivity and Lorentz force on the flow and heat transfer of a ferro-nanofluid in a magnetic field, Energies 10 (7) (2017), https://doi.org/10.3390/en10071065.

[48] J. Zhang, et al., Effect of tensile strain on thermal conductivity in monolayer graphene nanoribbons: a molecular dynamics study, Sensors (Switzerland) 13 (7) (2013) 9388–9395, https://doi.org/10.3390/s130709388.

[49] H.F. Lee, S. Kumar, M.A. Haque, Role of mechanical strain on thermal conductivity of nanoscale aluminum films, Acta Mater. 58 (20) (2010) 6619–6627, https://doi.org/10.1016/j.actamat.2010.08.024.

[50] K.P. Vemuri, F.M. Canbazoglu, P.R. Bandaru, Guiding conductive heat flux through thermal metamaterials, Appl. Phys. Lett. 105 (19) (2014), https://doi.org/10.1063/1.4901885.

[51] F. Lebeda, M. Demleitner, A. Pongratz, H. Ruckdäschel, M. Retsch, Shaping thermal transport and temperature distribution via anisotropic carbon fiber reinforced composites, ACS Omega 9 (37) (2024) 39232–39241, https://doi.org/10.1021/acsomega.4c06558.

[52] A. Mirabolghasemi, A.H. Akbarzadeh, D. Rodrigue, D. Therriault, Thermal conductivity of architected cellular metamaterials, Acta Mater. 174 (2019) 61–80, https://doi.org/10.1016/j.actamat.2019.04.061.

[53] Y. Aider, I. Kaur, H. Cho, P. Singh, Periodic heat transfer characteristics of additively manufactured lattices, Int. J. Heat Mass Transf. 189 (2022) 122692, https://doi.org/10.1016/j.ijheatmasstransfer.2022.122692.

[54] L. Qiu, X. Wang, G. Feng, Y. Feng, Tailorable thermal conduction and thermal energy storage behaviors in 3D printed hierarchical cellular structure-based phase change materials, Small Methods 9 (7) (2025) 1–12, https://doi.org/10.1002/smtd.202402089.

[55] J.S. Huang, C.Y. Wang, Numerical simulation and measurement of effective thermal conductivity of an additively manufactured lattice microstructure with gradient porosity, Results Eng. 25 (100) (2025) 104177, https://doi.org/10.1016/j.rineng.2025.104177.

[56] Y. Zhou, S. Shen, T. Liu, P. Li, F. Duan, Effective heat conduction evaluation of lattice structures from selective laser melting printing, Int. J. Heat Mass Transf. 218 (May 2023) (2024) 124790, https://doi.org/10.1016/j.ijheatmasstransfer.2023.124790.

[57] M. Sun, G. Yan, C. Hu, J. Zhao, F. Duan, Y. Song, Thermal and hydraulic behaviours of Kelvin cells from metallic three-dimensional printing, Appl. Therm. Eng. 219 (PA) (2023) 119433, https://doi.org/10.1016/j.applthermaleng.2022.119433.

[58] G. Yan, et al., Thermal-hydraulic performance of modified Schwartz-Diamond solid-networks triply periodic minimal surface structures, Appl. Therm. Eng. 249 (April) (2024) 123384, https://doi.org/10.1016/j.applthermaleng.2024.123384.

[59] H. Li, et al., Thermal effect of the anisotropic metal foam on the melting performance of phase change material: a pore-scale study, Int. Commun. Heat Mass Transf. 159 (PA) (2024) 107995, https://doi.org/10.1016/j.icheatmasstransfer.2024.107995.

[60] J. Yang, C. Liu, H. Xie, W. Yu, Anisotropic heat transfer properties of two-dimensional materials, Nanotechnology 32 (16) (2021), https://doi.org/10.1088/1361-6528/abdb15.

[61] L.K. Mao, R. Zhao, J. Chen, W.L. Cheng, Theoretical and experimental study on the anisotropic thermal conductivity of composite phase change materials prepared by hot-pressing method, Int. J. Heat Mass Transf. 198 (2022) 123380, https://doi.org/10.1016/j.ijheatmasstransfer.2022.123380.

[62] P. Guo, N. Sheng, R. Zhu, C. Zhu, Z. Rao, Improved anisotropic thermal transfer property of form-stable phase change material supported by 3D bionic porous copper, ACS Sustain. Chem. Eng. 11 (8) (2023) 3324–3333, https://doi.org/10.1021/acssuschemeng.2c06396.

[63] X. Zhang, et al., Enhanced melting behavior of phase change materials using anisotropic primitive sheet-networks triply periodic minimal surface structure, Energy 328 (November 2024) (2025) 136624, https://doi.org/10.1016/j.energy.2025.136624.

[64] H. Li, B. Chen, P. Zhu, C. Zhong, C. Ma, Study on phase-change heat transfer characteristics of anisotropic TPMS skeleton composite materials, Energy Storage Sci. Technol. 13 (12) (2024) 4319–4329.

[65] T. Zhang, K. Zhang, F. Liu, M. Zhao, D.Z. Zhang, Analysis of thermal storage behavior of composite phase change materials embedded with gradient-designed TPMS thermal conductivity enhancers: a numerical and experimental study, Appl. Energy 358 (October 2023) (2024) 122630, https://doi.org/10.1016/j.apenergy.2024.122630.

[66] Z. Yang, T. Zhang, W. Li, Y. Zhou, X. Li, F. Liu, Experimental and numerical assessments of thermal transport in phase change material embedding additively manufactured triply periodic minimal surfaces: a comparative evaluation, Appl. Therm. Eng. 245 (March) (2024) 122850, https://doi.org/10.1016/j.applthermaleng.2024.122850.

[67] D. Mirković, J. Gröbner, R. Schmid-Fetzer, Solidification paths of multicomponent monotectic aluminum alloys, Acta Mater. 56 (18) (2008) 5214–5222, https://doi.org/10.1016/j.actamat.2008.07.001.

[68] F. Riche, M. Schneebeli, Thermal conductivity of snow measured by three independent methods and anisotropy considerations, Cryosphere 7 (1) (2013) 217–227, https://doi.org/10.5194/tc-7-217-2013.

[69] A.R. Hadjesfandiari, On the symmetric character of the thermal conductivity tensor, Int. J. Mater. Struct. Integr. 8 (4) (2015) 209–220, https://doi.org/10.1504/IJMSI.2014.067111.

[70] M.H. Kourra, K. Sadki, L.B. Drissi, M. Bousmina, Mechanical response, thermal conductivity and phononic properties of group III-V 2D hexagonal compounds, Mater. Chem. Phys. 267 (April) (2021) 124685, https://doi.org/10.1016/j.matchemphys.2021.124685.

[71] M. Karkri, Effective thermal conductivity of composite: numerical and experimental study, in: COMSOL Conference, 2010.

[72] P. Jiang, X. Qian, X. Li, R. Yang, Three-dimensional anisotropic thermal conductivity tensor of single crystalline β-Ga_2O_3, Appl. Phys. Lett. 113 (23) (2018), https://doi.org/10.1063/1.5054573.

[73] S. Xu, J. Shen, S. Zhou, X. Huang, Y.M. Xie, Design of lattice structures with controlled anisotropy, Mater. Des. 93 (2016) 443–447, https://doi.org/10.1016/j.matdes.2016.01.007.

[74] E.B. Soboleva, Rayleigh-Darcy Convection in a Porous Layer: A Comparison of Near-critical and Normal Fluid Phases, 2010, p. 16. Available: http://arxiv.org/abs/1001.4139 (Online).

[75] O. Al-Ketan, R.K. Abu Al-Rub, MSLattice: a free software for generating uniform and graded lattices based on triply periodic minimal surfaces, Mater. Des. Process. Commun. 3 (6) (2021) 1–10, https://doi.org/10.1002/mdp2.205.

[76] R. Casati, M. Coduri, S. Checchia, M. Vedani, Insight into the effect of different thermal treatment routes on the microstructure of AlSi7Mg produced by laser powder bed fusion, Mater. Charact. 172 (January) (2021) 110881, https://doi.org/10.1016/j.matchar.2021.110881.

[77] R.A. Overfelt, S.I. Bakhtiyarov, R.E. Taylor, Thermophysical properties of A201, A319, and A356 aluminium casting alloys, High Temp. High Press. 34 (4) (2002) 401–409, https://doi.org/10.1068/htjr052.

[78] Thermo-calc, Thermo-Calc documentation set Thermo-Calc Version 2023a, Available: https://thermocalc.com/support/documentation/, 2023. (Accessed 21 January 2023) (Online).

[79] E. Yamasue, M. Susa, H. Fukuyama, K. Nagata, Deviation from Wiedemann–Franz law for the thermal conductivity of liquid tin and lead at elevated temperature, Int. J. 24 (3) (2003) 2–12.

[80] Z. Li, E. Gariboldi, Review on the temperature-dependent thermophysical properties of liquid paraffins and composite phase change materials with metallic porous structures, Mater. Today Energy 20 (2021), https://doi.org/10.1016/j.mtener.2021.100642.

[81] F. Zhou, S.N. Joshi, Y. Liu, E.M. Dede, Near-junction cooling for next-generation power electronics, Int. Commun. Heat Mass Transf. 108 (August) (2019) 104300, https://doi.org/10.1016/j.icheatmasstransfer.2019.104300.

[82] H. Xu, J. Huang, W. Tian, Z. Li, Thermal performance optimization of integrated microchannel cooling plate for IGBT power module, Micromachines 14 (8) (2023), https://doi.org/10.3390/mi14081498.

[83] L.Y. Li, et al., Revealing the mechanism of significant enhancement in interfacial thermal transport in silicon-based ceramic crystalline/amorphous matrix composite phase change materials, Rare Metals 44 (6) (2025) 4107–4118, https://doi.org/10.1007/s12598-025-03301-2.

[84] M. Molteni, S. Candidori, S. Graziosi, E. Gariboldi, Design of thermal conductivity, permeability, and heat storage behavior of composite phase change materials based on metallic TPMS lattices, Int. J. Heat Mass Transf. 241 (January) (2025) 126730, https://doi.org/10.1016/j.ijheatmasstransfer.2025.126730.

[85] A.J. Rawson, E. Kisi, C. Wensrich, Microstructural efficiency: structured morphologies, Int. J. Heat Mass Transf. 81 (2015) 820–828, https://doi.org/10.1016/j.ijheatmasstransfer.2014.11.012.

[86] E. Gariboldi, Z. Li, A.J. Rawson, Effective thermal conductivity in BCC and FCC lattices for all volume fractions and conductivity ratios: analyses by microstructural efficiency and morphology factor and analytic models, Mater. Today Commun. 33 (May) (2022) 104253, https://doi.org/10.1016/j.mtcomm.2022.104253.

[87] Y. Lu, W. Zhao, Z. Cui, H. Zhu, C. Wu, The anisotropic elastic behavior of the widely-used triply-periodic minimal surface based scaffolds, J. Mech. Behav. Biomed. Mater. 99 (2) (2019) 56–65, https://doi.org/10.1016/j.jmbbm.2019.07.012.

[88] J. Ordóñez-Miranda, J.J. Alvarado-Gil, R. Medina-Ezquivel, Generalized Bruggeman formula for the effective thermal conductivity of particulate composites with an interface layer, Int. J. Thermophys. 31 (4–5) (2010) 975–986, https://doi.org/10.1007/s10765-010-0756-2.

[89] B. Raghava Rao, V. Ramachandra Raju, K. Mohana Rao, Effect of fibre shape on transverse thermal conductivity of unidirectional composites, Sadhana Acad. Proc. Eng. Sci. 40 (2) (2015) 503–513, https://doi.org/10.1007/s12046-014-0323-9.

[90] Y. Takao, M. Taya, The effect of variable fiber aspect ratio on the stiffness and thermal expansion coefficients of a short fiber composite, J. Compos. Mater. 21 (2) (1987) 140–156, https://doi.org/10.1177/002199838702100205.

[91] T. Evgin, et al., Effect of aspect ratio on thermal conductivity of high density polyethylene/multi-walled carbon nanotubes nanocomposites, Compos. Part A Appl. Sci. Manuf. 82 (2016) 208–213, https://doi.org/10.1016/j.compositesa.2015.12.013.

[92] H. Altendorf, D. Jeulin, F. Willot, Influence of the fiber geometry on the macroscopic elastic and thermal properties, Int. J. Solids Struct. 51 (23–24) (2014) 3807–3822, https://doi.org/10.1016/j.ijsolstr.2014.05.013.

[93] K. Amara, M.Z. Saghir, R. Abdeljabar, Review of triply periodic minimal surface (TPMS) structures for cooling heat sinks, Energies 18 (18) (2025) 1–26, https://doi.org/10.3390/en18184920.

[94] V. Shevchenko, S. Balabanov, M. Sychov, L. Karimova, Prediction of cellular structure mechanical properties with the geometry of triply periodic minimal surfaces (TPMS), ACS Omega 8 (30) (2023) 26895–26905, https://doi.org/10.1021/acsomega.3c01631.